






RESEARCH ARTICLE

10.1029/2020JD033015

Measurements of Tropospheric Bromine Monoxide Over Four Halogen Activation Seasons in the Canadian High Arctic

K. Bognar¹ , X. Zhao² , K. Strong¹ , R. Y.-W. Chang³ , U. Frieß⁴, P. L. Hayes⁵ , A. McClure-Begley⁶, S. Morris⁶, S. Tremblay⁵, and A. Vicente-Luis⁵

¹Department of Physics, University of Toronto, Toronto, Ontario, Canada, ²Air Quality Research Division, Environment and Climate Change Canada, Toronto, Ontario, Canada, ³Department of Physics and Atmospheric Science, Dalhousie University, Halifax, Nova Scotia, Canada, ⁴Institute of Environmental Physics, University of Heidelberg, Heidelberg, Germany, ⁵Department of Chemistry, University of Montreal, Montreal, Quebec, Canada, ⁶NOAA Earth System Research Laboratory, Boulder, CO, USA

Key Points:

- High wind speeds lead to enhanced tropospheric BrO with little to no ozone depletion
- Snow on first-year ice and multiyear ice likely both contribute to observed BrO enhancements
- High coarse-mode (>0.5 μm) aerosol load is necessary and sufficient to maintain enhanced BrO aloft

Supporting Information:

- Supporting Information S1

Correspondence to:

K. Bognar and K. Strong,
kbognar@atmosph.physics.utoronto.ca;
strong@atmosph.physics.utoronto.ca

Citation:

Bognar, K., Zhao, X., Strong, K., Chang, R. Y.-W., Frieß, U., Hayes, P. L., et al. (2020). Measurements of tropospheric bromine monoxide over four halogen activation seasons in the Canadian high Arctic. *Journal of Geophysical Research: Atmospheres*, 125, e2020JD033015. <https://doi.org/10.1029/2020JD033015>

Received 30 APR 2020

Accepted 27 AUG 2020

Accepted article online 4 SEP 2020

Abstract Bromine explosions and corresponding ozone depletion events are common in the Arctic spring. The snowpack on sea ice and sea salt aerosols (SSA) are both thought to release bromine, but the relative contribution of each source is not yet known. Furthermore, the role of atmospheric conditions is not fully understood. Long-term measurements of bromine monoxide (BrO) provide useful insight into the underlying processes of bromine activation. Here we present a 4-year data set (2016–2019) of springtime BrO partial columns retrieved from Multi-AXis Differential Optical Absorption Spectroscopy (MAX-DOAS) measurements in Eureka, Canada (80.1°N, 86.4°W, 610 m asl). Due to the elevation of the measurement site, the instrument often measures BrO in the free troposphere, except during strong wind episodes and storms that generate a deep boundary layer. Enhanced vertical mixing due to strong winds leads to increasing BrO values and reduced ozone depletion. We find that BrO enhancements show two modes differentiated by local wind direction and air mass history. Longer time spent by the airmass in first-year sea ice areas corresponds to increased BrO for one of these modes only. Furthermore, we argue that snow on multiyear ice might also contribute to bromine release. High aerosol optical depth is required to maintain lofted BrO, and we show that the presence of coarse-mode aerosols (>0.5 μm, likely SSA) is a necessary and sufficient condition for observing BrO at our elevated measurement site in Eureka. This work highlights the importance of considering variable local conditions when characterizing bromine activation.

1. Introduction

Halogens play an important role in the Arctic troposphere. Reactive bromine species (Br and BrO) are responsible for ozone depletion events (ODEs; Barrie et al., 1988; Bottenheim et al., 1986; Oltmans & Komhyr, 1986), which are frequent reductions of near-surface ozone to very low levels during the months of March to May. ODEs occur mostly over the frozen Arctic Ocean, and ozone-depleted airmasses can extend over hundreds of km horizontally (e.g., Halfacre et al., 2014). Bromine chemistry also leads to mercury deposition, with potentially harmful impacts on the Arctic environment (Berg et al., 2013; Cole & Steffen, 2010; Schroeder et al., 1998; Steffen et al., 2008). Bromine is thought to be released to the atmosphere from condensed phase bromide (Br⁻) through heterogeneous reactions (Eigen & Kustin, 1962; Fan & Jacob, 1992; Wang et al., 2019).

The heterogeneous release of bromine, combined with the reaction of bromine with ozone, creates an autocatalytic reaction cycle that can lead to the sudden buildup of reactive bromine in the atmosphere, during events often referred to as “bromine explosions” (Wennberg, 1999). The mechanisms involved in bromine release are the subject of several recent reviews (Abbatt et al., 2012; Saiz-Lopez & von Glasow, 2012; Simpson et al., 2015). BrO, detectable using remote sensing, is commonly used as an indicator of bromine activation, since it is produced from the ozone destruction cycle. The lifetime of BrO is on the order of minutes due to photolysis, but Br and BrO are rapidly cycled at normal ozone levels. Once ozone is completely depleted, however, BrO cannot form and bromine might be converted to more stable species, or the bromine explosion might continue via reactions with nitrogen oxides (Wang et al., 2019).

The surfaces involved in the heterogeneous bromine release are a topic of ongoing research. The snowpack on first-year ice (FYI) and on land has long been considered a potential source of bromine (e.g. Foster et al., 2001; Spicer et al., 2002). Using outdoor snow chambers, Pratt et al. (2013) measured emission of molecular bromine when snow samples were exposed to sunlight. They found that this process was most efficient for more acidic samples in the presence of ozone, consistent with the bromine explosion mechanism. Wren et al. (2013) arrived at similar conclusions from laboratory experiments. Flux measurements of molecular bromine from the tundra snowpack by Custard et al. (2017) indicated that the snowpack is potentially a dominant source of bromine to the atmosphere. Bromine release from the snowpack often occurs in the presence of weak winds and a shallow, stable boundary layer. Multi-AXis Differential Optical Absorption Spectroscopy (MAX-DOAS; Hönninger et al., 2004) measurements indicate that bromine in such conditions is restricted to the lowest 200–300 m of the atmosphere (Peterson et al., 2015; Simpson et al., 2017). Wind pumping by moderate winds enhances the transfer of bromine from the snowpack to the atmosphere (Peterson et al., 2015; Pratt et al., 2013), and strong temperature inversions typical in the Arctic spring inhibit vertical mixing. This allows bromine to build up and destroy ozone near the surface. Measurements over the Arctic Ocean showed that most of the marine boundary layer is likely to be at least partially depleted of ozone in the spring (Halfacre et al., 2014; Jacobi et al., 2010).

Other potential sources of bromine include blowing snow and aerosol particles. Yang et al. (2008) and Jones et al. (2009, 2010) argued that high wind speeds and good mixing conditions might create another set of favorable conditions for bromine release. This is in agreement with the recent results of Swanson et al. (2020), who found that the statistics of BrO measurements across the Arctic differentiate into the two sets of environmental conditions outlined above. Strong winds ($7\text{--}8\text{ m s}^{-1}$, Li & Pomeroy, 1997) generate blowing snow, and these particles might release bromine through a process similar to what is observed in the snowpack. MAX-DOAS measurements by Frieß et al. (2011) and in situ measurements by Liao et al. (2012) indicated that BrO levels were higher at faster wind speeds ($5\text{--}6\text{ m s}^{-1}$). Other studies, however, did not observe such a relationship (Peterson et al., 2015). It is important to note, however, that blizzard conditions can significantly lower the sensitivity of MAX-DOAS measurements to BrO (Frieß et al., 2011). In situ analysis of blowing snow in Antarctica provided a range of results, with Br[−] depletion (compared to seawater) reported by Lieb-Lappen and Obbard (2015), Br[−] enrichment reported by Hara et al. (2018), and a range of values (small to no depletion on average) observed by Frey et al. (2020).

While the direct role of blowing snow is uncertain, sea salt aerosol (SSA) might act as a source of bromine to the atmosphere. In the absence of open ocean in the Arctic winter and spring, sources of SSA include sublimation of blowing snow (Frey et al., 2020; Giordano et al., 2018; Huang & Jaeglé, 2017; Huang et al., 2018; Yang et al., 2008; Zhao et al., 2017) and leads in sea ice (Kirpes et al., 2019; Leck et al., 2002; May et al., 2016; Nilsson et al., 2001). Enhanced aerosol extinction was found to correlate with increased BrO concentrations measured by MAX-DOAS (Frieß et al., 2011; Peterson et al., 2015; Simpson et al., 2017; Swanson et al., 2020), although Simpson et al. (2017) noted that high extinction was necessary but not sufficient to maintain BrO aloft. Peterson et al. (2017) reported aircraft measurements of a lofted BrO plume maintained by bromine recycling on supermicron aerosol particles. In situ measurements by Hara et al. (2002) in Ny-Ålesund, Svalbard, showed Br[−] depletion in coarse-mode SSA ($>2\text{ }\mu\text{m}$) and Br[−] enhancement in the fine mode. Recent in situ measurements from Antarctica provide further evidence about the role of SSA in bromine release. Legrand et al. (2016) observed significant Br[−] depletion in supermicron SSA in the spring and Br[−] enhancement in submicron particles. Hara et al. (2018) found springtime SSA to be depleted in Br[−] in all size bins. Using measurements at altitudes of 2 m and at 29 m above the surface, Frey et al. (2020) found that, while individual measurements showed some scatter, SSA at 29 m generally showed strong depletion in bromide, whereas SSA at 2 m usually showed strong enrichment. The authors concluded that surface snow, blowing snow, and aerosols likely all participate in bromine recycling, and aerosols likely contribute a significant amount of bromine to the atmosphere.

Satellite measurements of tropospheric BrO appear to confirm the role of SSA in bromine release. Modeled BrO release from SSA has been found sufficient to explain measurements from the Global Ozone Monitoring Experiment (GOME) and GOME-2 satellite instruments (e.g., Theys et al., 2011; Yang et al., 2010), and Arctic cyclones with high surface winds have been linked to large BrO plumes seen in GOME-2 data (Begoïn et al., 2010; Blechschmidt et al., 2016; Sihler et al., 2012; Zhao et al., 2016). More recently, Choi et al. (2018) showed that tropospheric BrO columns from the Ozone Monitoring Instrument (OMI) correlated with modeled SSA emissions in the Arctic, while bromine explosion frequency showed little to no correlation with

FYI area. However, as often noted in the literature, the detection of shallow boundary layer BrO events (typical for snowpack bromine release) is not straightforward for nadir-viewing satellite instruments (GOME, GOME-2, and OMI), given the need to separate the tropospheric BrO column from the total column (e.g., Sihler et al., 2012). Visibility of BrO from space increases for distributed BrO events in a deeper mixing layer, which are often associated with bromine activation on aerosols. As a result of this discrepancy between the sensitivities of ground-based and satellite measurements, the relative importance of the snowpack and SSA to the bromine budget in the Arctic troposphere remains uncertain.

This study presents 4 years (2016–2019) of MAX-DOAS BrO measurements from Eureka, Canada (80.1°N, 86.4°W). We use retrieved partial columns from four bromine activation seasons (March through May) to investigate the environmental controls on BrO in Eureka. We seek to better understand the role of local meteorology in bromine activation, as well as the relative contributions of the snowpack and SSA. Our data set is a valuable addition to the discussion, since there are few other long-term ground-based BrO data sets described in the literature. In addition, the elevation of the measurement site (610 m) means that the MAX-DOAS instrument is often located above the boundary layer. This presents an interesting opportunity to examine free tropospheric BrO from a ground-based station.

The paper is structured as follows: The measurement site, the MAX-DOAS instrument, the BrO retrievals, and additional data sets used in this study are discussed in section 2. Section 3.1 includes an overview of the BrO data set and the related variables, with a focus on year-to-year and month-to-month variability. The history of the air masses over the entire study period is examined in section 3.2. Section 4 delves deeper into the relationships between BrO and environmental variables, including wind speed, stability, and temperature (section 4.1), sea ice sensitivity along back trajectories (section 4.2), and in situ aerosol concentrations (section 4.3). The conclusions are given in section 5.

2. Methods and Data Sets

2.1. Measurement Site and Local Meteorology

The measurements in this study were collected at the Polar Environment Atmospheric Research Laboratory (PEARL) in Eureka, Canada (Fogal et al., 2013). PEARL and the Environment and Climate Change Canada (ECCC) Eureka Weather Station (EWS) host a suite of remote sensing and in situ instruments that can be used to probe halogen chemistry in the Arctic. PEARL is a collection of three separate facilities operated by the Canadian Network for the Detection of Atmospheric Change (CANDAC) since 2005. The main facility is the PEARL Ridge Laboratory, located approximately 15 km from EWS, at an altitude of 610 m above sea level. The MAX-DOAS instrument and the aerosol instruments are located in the PEARL Ridge Lab. The surface ozone monitor is located at the Zero-Altitude PEARL Auxiliary Laboratory (OPAL) within EWS at 10 m altitude.

The EWS facilities are located on the shore of small fjord, while the PEARL Ridge Lab is somewhat further from the coast, as shown in Figure 1. The region is characterized by mountainous terrain typical for Ellesmere Island. Fjords cutting through the island provide natural channels for airflow in the stable atmospheric conditions of winter and spring. While Eureka is around 200 km away from the Arctic Ocean, the wide Nansen Sound (Figure 1) often guides airmasses from the Arctic Ocean directly to the site. During winter and spring, the fjords around Eureka and the waters near Ellesmere Island are covered by FYI. The Arctic Ocean just north of Ellesmere Island is usually covered by multiyear ice (MYI). EWS and the PEARL Ridge Lab might not always sample the same air masses, due to reasons discussed below.

Radiosondes are launched twice daily from EWS. Temperature profiles indicate that a strong inversion is present most of the time from March through May. Every sonde from the four spring seasons considered here shows a temperature difference between the surface and the altitude of the PEARL Ridge Lab that is less than the dry adiabatic lapse rate. Exceptions to these stable conditions include stormy days with near-zero temperature gradients, signifying a well-mixed atmosphere. It is likely that aside from storms, remote sensing instruments located in the PEARL Ridge Lab measure above the boundary layer in the spring. The impact of atmospheric stability on in situ measurements is less clear, due to the unknown impact of local terrain on the boundary layer. The comparison of in situ temperature measurements from EWS and the PEARL Ridge Lab, however, shows temperature differences similar to the radiosonde measurements.

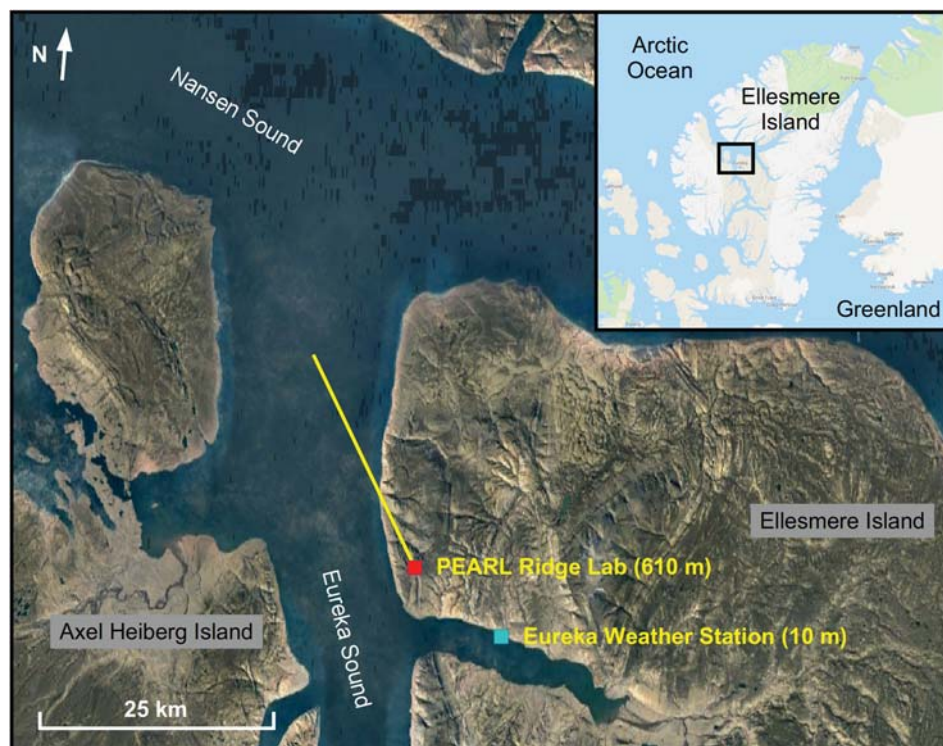


Figure 1. Location of the PEARL Ridge Lab and the Eureka Weather Station. The small insert shows the location of the main map on Ellesmere Island, Canada. The yellow line (25 km in length) represents the MAX-DOAS viewing direction of 330°. Images: Google Earth/Google Maps.

Figure 2 shows the distribution of springtime (March–May) winds for 2016–2019, measured at the PEARL Ridge Lab (610 m altitude). The wind rose shows a clear bimodal distribution, where winds come from the north close to 50% of the time, and southeasterly winds account for another quarter of the observations. The southeasterly winds show a larger fraction of strong winds compared to northerly winds, due to storms that usually come in from the southeast. The same wind patterns appear in the wind data from EWS at 10 m altitude as well (data not shown). To examine the effect of wind direction on bromine activation, all data were analyzed as a function of wind direction. The wind direction bins were selected as $354^\circ \pm 30^\circ$ for northerly (N) winds and $123^\circ \pm 30^\circ$ for southeasterly (SE) winds, with the remaining wind directions categorized as “other.” The mean wind direction of each bin was determined using a Gaussian fit to the wind direction histogram.

2.2. MAX-DOAS Measurements

The MAX-DOAS measurements of BrO and oxygen dimer (O_4) used in this study were made using the PEARL Ground-Based Spectrometer (PEARL-GBS) (Fraser et al., 2009), located in the PEARL Ridge Lab. The PEARL-GBS is a Jobin-Yvon/Horiba Triax-180 crossed Czerny-Turner imaging spectrometer. Spectra are recorded using a thermoelectrically cooled (201 K), back-illuminated charge-coupled device (CCD) detector, with 2048×512 pixels and a UV-enhanced coating. The 512 vertical CCD pixels are averaged for the measurements. The spectrometer is coupled to a suntracker (installed outside, under a UV-transparent acrylic dome) to allow multiple viewing geometries. The suntracker consists of two UV-enhanced aluminum mirrors that direct the light, through a focusing lens, to the spot end of a 30 m spot-to-slit optical fiber bundle (37 fibers). The instrument has a field-of-view of approximately 1° , and measurements consist of the average of 100 individual spectra, recorded over 1.5 to 3 min, depending on light conditions.

PEARL-GBS measurements from 2016 to 2019 (spring data only) were used in this study. MAX-DOAS spectra were recorded in the UV (320–400 nm) using a 1,200 grooves per mm grating that provides a resolution of 0.45–0.5 nm across the selected wavelength range. Elevation angles of -1° , 1° , 2° , 5° , 10° , 15° , 30° , and 90° were used in each MAX-DOAS scan. The constant azimuth viewing direction of 330° (clockwise from

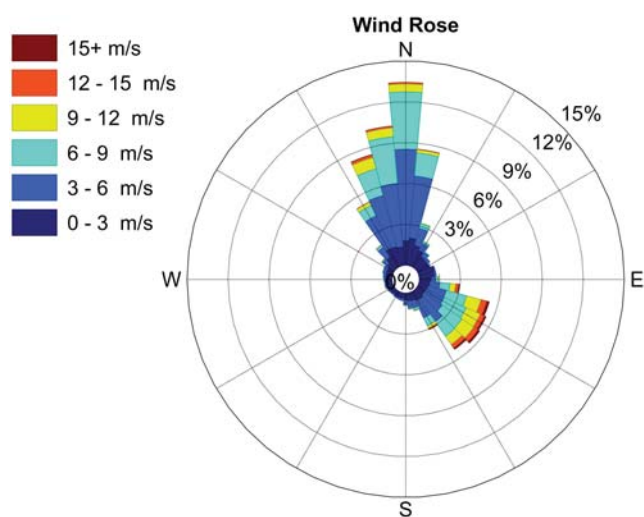


Figure 2. Wind rose for March–May using wind speed and wind direction measured at the PEARL Ridge Lab (610 m altitude) from 2016 to 2019.

north, see Figure 1) points down a valley that extends from the PEARL Ridge Lab to the nearby fjord, therefore allowing an unobstructed line-of-sight for the low elevation angle measurements (Figure S1 in the supporting information). Spectra are recorded for solar elevations above 4° , and so the daily measurement window varies from a few hours in early March to nearly 20 hr by May. Spectra are not recorded while the solar azimuth is close to the azimuth viewing direction of the instrument.

Spectra were analyzed using the QDOAS software (Danckaert et al., 2017). Differential slant column densities (dSCDs) of BrO and O_4 were retrieved using the cross sections and settings shown in Table 1 of Zhao et al. (2016). The reference spectra for the DOAS analysis were interpolated to the time of the given off-axis measurement from the zenith-sky measurements taken immediately before and after the current scan.

PEARL-GBS MAX-DOAS measurements are available as far back as 2010 (e.g., Zhao et al., 2016), but data prior to 2016 were excluded due to the variable sets of elevation angles used. The lowest available viewing angle prior to 2016 was limited to 5° by the old location of the suntracker, and so the data are less useful for profile retrievals, especially in low BrO conditions.

2.3. BrO Profile Retrieval

To obtain the BrO partial columns and aerosol optical depths (AODs) used in this study, the MAX-DOAS dSCDs were first converted to profiles using the optimal estimation method (Rodgers, 2000). Optimal estimation determines the most probable atmospheric state given the set of dSCDs and a priori information. A radiative transfer model is used as the forward model to simulate dSCDs given the estimated trace gas concentrations and other atmospheric parameters (e.g., pressure and temperature profiles) that are not retrieved. The modeled dSCDs are compared to the measured values, taking into account the error covariance matrices for the measurements and for the a priori profile. The estimated atmospheric conditions are then adjusted, and this process is iterated until the cost function reaches a prescribed minimum value. The sensitivity of the retrieved profiles to the true state of the atmosphere is described by the averaging kernel matrix, and the trace of the averaging kernel gives the degrees of freedom for signal (DOFS). The DOFS represents the number of independent pieces of information contained in the retrieval.

Here we use the Heidelberg remote sensing group profile retrieval code (HEIPRO; Frieß et al., 2011; Yilmaz, 2012). The code uses the radiative transfer model SCIATRAN (Rozanov et al., 2005) as the forward model. HEIPRO follows a two-step retrieval approach, where the aerosol extinction profiles are first retrieved from O_4 dSCDs, and then, in the second step, the extinction profiles are used as a forward model parameter for the BrO profile retrieval. Profiles were retrieved in the lowest 4 km of the atmosphere, on a 200 m altitude grid.

Following Frieß et al. (2011), we use two iteration runs in the aerosol extinction retrieval, with five iteration steps in each (the retrieved state from the first iteration run was used as the starting point of the second iteration run). We found that using a larger number of iteration steps sometimes resulted in unrealistic profiles. For the retrieval, the single scattering albedo was fixed at 0.95, and the asymmetry parameter (for the Henyey-Greenstein phase function) was set to 0.72, to account for a variety of aerosol conditions. We used an exponential a priori extinction profile, with surface extinction of 0.05 km^{-1} and a scale height of 2 km (Zhao et al., 2016). The BrO profiles were retrieved in a single iteration run (10 iteration steps). The BrO a priori profile was set to an exponential, with a surface concentration of 5 pptv and a scale height of 0.5 or 1 km (similar to Zhao et al., 2016). The scale height was set according to conditions of atmospheric stability, 0.5 km for strong inversions (inversion strength at 610 m $\geq 7^\circ\text{C}$) and 1 km for weaker inversions. The diagonal elements of the a priori error covariance matrix (in both the extinction and the BrO retrievals) were set to twice the values in the a priori profile, and the off-diagonal elements were set to decrease exponentially with a correlation length of 500 m. Retrievals were performed using fixed a priori conditions for each (UTC) day, and variable a priori parameters (scale height of the BrO a priori profile, temperature and pressure profiles from radiosonde data, and ozone profiles from ozonesonde data) were recalculated for each day.

Only the 0–4 km BrO partial columns and the retrieved AODs were used in this study. We decided not to include profile information due to the potential impacts of retrieval parameters on the BrO profile shape. Like previous studies (Peterson et al., 2015; Zhao et al., 2016), we found that the retrieved BrO profiles were sensitive to the selection of the a priori profile scale height. The BrO concentrations were largest in the lowest few hundred meters for a priori profiles with a scale height of 0.5 km, while BrO was more evenly distributed for a priori profiles with a 1 km scale height. The partial columns, on the other hand, are relatively insensitive to changes in the retrieved vertical distribution of BrO. Sensitivity tests showed that changing the value of the scale height (0.5 to 1 km and vice versa) only has a 5–10% influence on the partial column results. We think that for the present study, the 0–4 km partial column values are the best representation of the amount and variability of BrO detected by the MAX-DOAS instrument.

Given the list of elevation angles and the altitude of the measurement site, we expect that the instrument is mostly sensitive to lofted BrO layers. Averaging kernels (Figure S1) show maximum sensitivity in the 600 m layer (near the altitude of the instrument). The BrO averaging kernels show little sensitivity above 1.5–2 km, regardless of the a priori scale height used. This sensitivity range is similar to results from Frieß et al. (2011) and Peterson et al. (2015). Estimating a lower limit for the sensitivity of BrO partial columns is less straightforward. Assuming a maximum horizontal sensitivity range of 10–15 km in the UV (e.g., Wagner et al., 2011), the -1° elevation angle line-of-sight would reach down to 350–450 m above sea level (or ~ 100 m lower when accounting for the 1° field-of-view). This is in general agreement with the averaging kernels, which usually show a broad peak between the 200 and 400 m levels. It's important to note that the retrieval considers an instrument floating at 610 m over flat terrain, and the topography around the measurement site is not taken into account. The -1° measurement looks down a valley that extends 9 km from the measurement site to the frozen Arctic Ocean. Given the bright snow cover over the valley, part of the light in the low elevation angle measurements is likely reflected from the floor and walls of the valley, enhancing the sensitivity to layers below the instrument altitude. Much of the valley, however, is significantly above sea level (the first 6 km along the line-of-sight is above 300 m) and is covered by only a thin (few cm) layer of snow. Some of the reflected light we measure might come from the sea ice farther along the line-of-sight, but we cannot quantify the exact sources of reflected light. Given the variable viewing conditions and the unknown effects of topography on the radiative transfer calculations, the BrO partial columns are likely most sensitive to altitudes above 300–500 m and below 1.5–2 km. As a result, the retrievals likely miss shallow BrO events and detect distributed and lofted events only.

Typical DOFS for the BrO retrievals were between 2 and 3, while aerosol DOFS were often between 3 and 4. To preserve information content, retrievals where either the aerosol or BrO DOFS were smaller than 0.7 were discarded (Payne et al., 2009; Peterson et al., 2015). In addition, a few remaining retrievals with $\text{AOD} > 5$ were removed (likely whiteout conditions or snow on the dome obstructing the input optics). After applying these filters, the mean DOFS for BrO partial columns is 2.27, with a standard deviation of 0.45, while the mean DOFS for AODs is 3.28, with a standard deviation of 0.70. The mean absolute uncertainty on the BrO partial columns is 4.7×10^{12} molec cm^{-2} (45.7% mean relative uncertainty). The mean relative uncertainty is heavily weighted by the smaller partial columns. The mean uncertainties for measurements above and below the median are 5.0×10^{12} molec cm^{-2} (24.4%) and 4.4×10^{12} molec cm^{-2} (66.9%), respectively. The mean uncertainty on the AOD values is 0.036 (38.5% mean relative uncertainty). To estimate an approximate detection limit for the BrO partial columns, we retrieved BrO profiles for 10 days in August 2018 (with variable aerosol conditions). Using a Gaussian fit to the distribution of partial columns, the 3σ detection limit was estimated to be 6.6×10^{12} molec cm^{-2} . This is a conservative estimate, assuming that no BrO is present in August. This assumption is reasonable in light of late summer conditions (temperatures above freezing, small sea ice extent) but ignores any potential free tropospheric BrO background. In fact, slight enhancements of BrO (up to $8\text{--}10 \times 10^{12}$ molec cm^{-2}) appear even in the August profile results.

2.4. Complementary Data Sets

Weather observations were recorded at EWS (hourly) and at the PEARL Ridge Lab (every minute). For most comparisons, we use weather data from the PEARL Ridge Lab, since those are higher frequency measurements colocated with the aerosol measurements and, to a lesser extent, with the MAX-DOAS measurements. Throughout this paper, references to meteorological variables indicate data from the PEARL Ridge Lab, unless specified otherwise. Ozonesondes (used in the BrO retrievals) were launched once per week from

EWS, with increased launch frequency in early March. Radiosondes were launched twice daily from EWS. Surface ozone measurement were made by a TFS 49i ozone analyzer located at OPAL (10 m altitude). Hourly mean surface ozone data are available for 2017–2019, since the instrument was installed in late 2016.

In situ aerosol measurements were made by three instruments located in the PEARL Ridge Lab (Tremblay et al., 2019; Vicente-Luis et al., 2020). Coarse-mode aerosol particles, defined here as diameters (d_p) greater than $0.5 \mu\text{m}$, were measured by an Optical Particle Counter (OPC, 3 min resolution, data available for 2016–2018), and an Aerodynamic Particle Sizer (APS, 1 min resolution, data available for 2019). The OPC measures the number concentration of particles with d_p between 0.3 and $20 \mu\text{m}$ in six size bins, while the APS measures aerodynamic particle diameters between 0.5 and $20 \mu\text{m}$ in 52 size bins. To combine the coarse-mode aerosol data into one time series, we assumed the OPC diameter is equal to the physical diameter (Tremblay et al., 2019) and merged integrated APS number concentrations with integrated OPC data for $d_p > 0.5 \mu\text{m}$. Owing to the lack of information about the shape and density of the particles measured by the APS, we assumed that the aerodynamic diameter is equal the physical diameter. Accumulation-mode aerosols were measured using a Scanning Mobility Particle Sizer (SMPS, data available for 2016–2019). Number concentrations were integrated for $0.1 \mu\text{m} < d_p < 0.5 \mu\text{m}$ (hereafter, this range is referred to as the accumulation mode).

Back trajectories and surface sensitivities were calculated using the FLEXible PARTicle (FLEXPART) model (Pisso et al., 2019; Stohl et al., 1998). FLEXPART is a Lagrangian particle dispersion model that can be used to simulate the transport and mixing of gases and aerosols in the atmosphere, both forward and backward in time. We calculated 3-day back trajectories by initializing FLEXPART at approximately 3-hr intervals during the periods when BrO partial columns were available. Passive tracer particles were released instantaneously in a 3° longitude by 0.8° latitude by 2 km altitude box, approximately centered on the sensitivity region of the MAX-DOAS measurements. We used 6-hourly meteorological fields ($0.5^\circ \times 0.5^\circ$ spatial resolution) from the Climate Forecast System (CFS V2) model simulations (Saha et al., 2011) provided by the National Centers for Environmental Prediction to calculate back trajectories.

The output of the backward FLEXPART simulations is sensitivity to emissions at the surface, at 1-hr time steps along the 3-day back trajectory. For each back trajectory, we calculate the total sensitivity in each grid cell (sum of the sensitivities for each time step) and record the mean trajectory, calculated using a clustering algorithm (Stohl et al., 2002). Since the surface sensitivities are calculated for the entire domain (Northern Hemisphere, $0.5^\circ \times 0.5^\circ$ resolution), we can obtain a measure of the amount of contact between the air masses and snow on FYI or MYI. For this purpose, we use weekly Equal-Area Scalable Earth (EASE) Grid ($12.5 \text{ km} \times 12.5 \text{ km}$) sea ice age data (Tschudi et al., 2019) from the National Snow and Ice Data Center at NASA. Maps of sea ice extent and age for the measurement period in each year are shown in Figure S3. To calculate FYI or MYI sensitivity for each back trajectory, we linearly interpolated the FLEXPART sensitivities to a fine grid ($0.01^\circ \times 0.025^\circ$, approximately $1 \text{ km} \times 1 \text{ km}$ or better in the Arctic) and converted the fine grid coordinates to the equal area projection of the sea ice data. Using this converted grid, we calculated the mean sensitivity within each sea ice cell. The weekly sea ice data were not interpolated, and back trajectories that spanned parts of 2 weeks were split up for the sea ice sensitivity calculations (and merged again later). Since the sea ice grid cells preserve area, the sea ice sensitivity for each back trajectory is then the sum of the sensitivities in each sea ice cell tagged as FYI or MYI.

To match high-frequency wind data and aerosol measurements to the BrO columns, average values were calculated for the mean measurement time of each BrO column, using the time interval of the MAX-DOAS measurements used in each profile retrieval (10–25 min). Note that wind speed and wind direction measurements are not available for approximately 4% of the BrO partial columns. We chose not to fill these gaps with EWS data, because while the overall statistics of wind measurements are similar at EWS and at the PEARL Ridge Lab, wind directions (as defined in section 2) calculated for individual BrO partial columns differ between the two for 70% of the data set. Low-frequency data sets, such as hourly measurements or the radiosonde data, were linearly interpolated to the time of the BrO partial columns. Sea ice sensitivity values calculated from FLEXPART back trajectories (one value every $\sim 3 \text{ hr}$) were linearly interpolated by day, with the values just before (after) the first (last) FLEXPART time of the day held constant. This was done in order to avoid interpolating between sea ice sensitivity values from separate days.

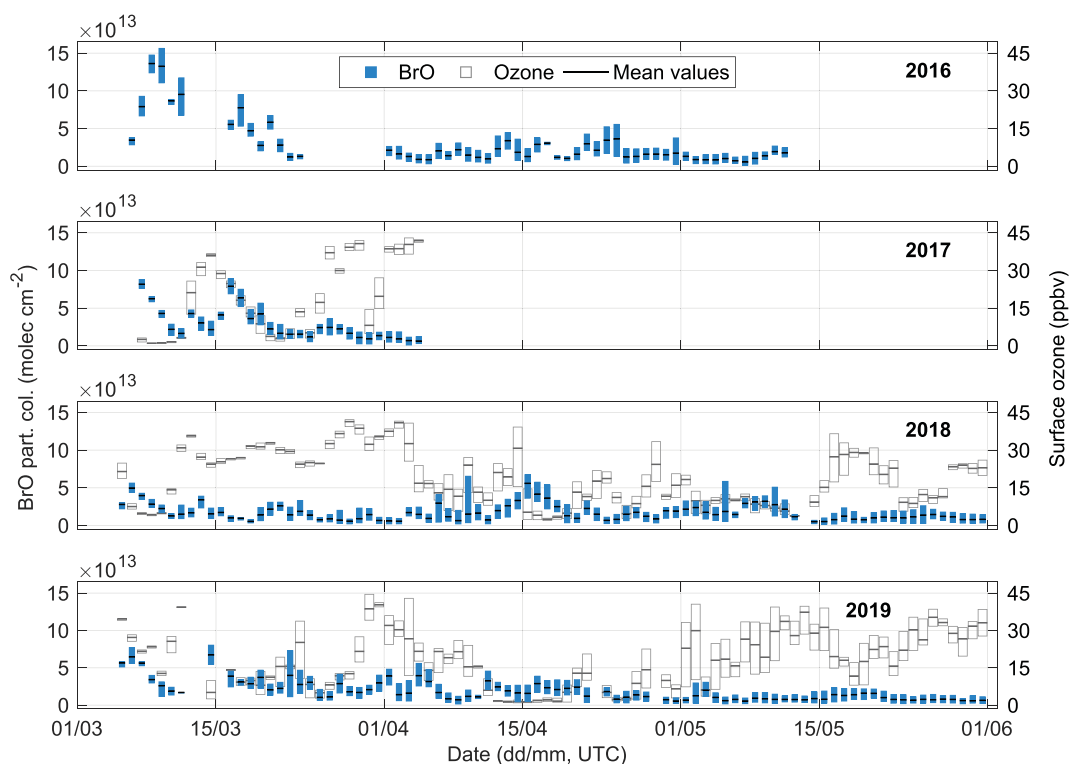


Figure 3. Daily range of retrieved 0–4 km BrO partial columns (blue rectangles) and paired surface ozone values (empty rectangles) for March to May 2016–2019. The rectangles represent the full range of values for each day, and the black lines show the daily mean.

3. Overview of the Data Set

3.1. Four Years of Springtime BrO Measurements

To understand the environmental controls on BrO variability, it is useful to first take a look at the time series of BrO and other closely related measurements. The 4 years of springtime observations presented here (254 days and over 10,000 partial columns) provide enough data to examine the month-to-month and year-to-year variability of bromine activation in Eureka.

Figure 3 shows the daily mean and range of BrO partial columns for the entire data set (March–May measurements) used in this study. Missing days (e.g., in March 2016 or 2019) typically indicate that the retrievals failed due to unfavorable weather (blizzards and whiteout conditions), while longer missing periods (e.g., April–May 2017) are due to instrument downtime. The largest BrO partial columns are observed in March, with some bromine activation in April and generally small BrO partial columns by May. The May measurements are often near or below the approximate detection limit. We did not define an end date for the bromine activation season each year (unlike, e.g., Burd et al., 2017), but used 31 May (or the last measurement date) instead. Excluding the typically low BrO partial columns in late May does not have a significant impact on the results presented here. On the other hand, May measurements provide a useful test to determine whether the observed relationships of BrO and other variables hold for background BrO conditions as well.

The month-to-month variability of the BrO partial columns is more readily apparent in Figure 4a. The mean and median, as well as the largest BrO partial columns, generally decrease from March through May, with March data showing the greatest variability. These patterns are typical for the bromine activation season. The year 2018 stands out: BrO concentrations were very low in March, and several BrO enhancements were observed in May. The low BrO partial columns in March 2018 correspond to low AOD and low coarse-mode aerosol concentrations (Figures 4b and 4d, respectively), as well as unusually high surface ozone measurements (Figure 4c). The year-to-year variability of BrO (especially in March) is in line with Swanson et al. (2020), who showed that springtime BrO in the Arctic exhibits significant interannual variability.

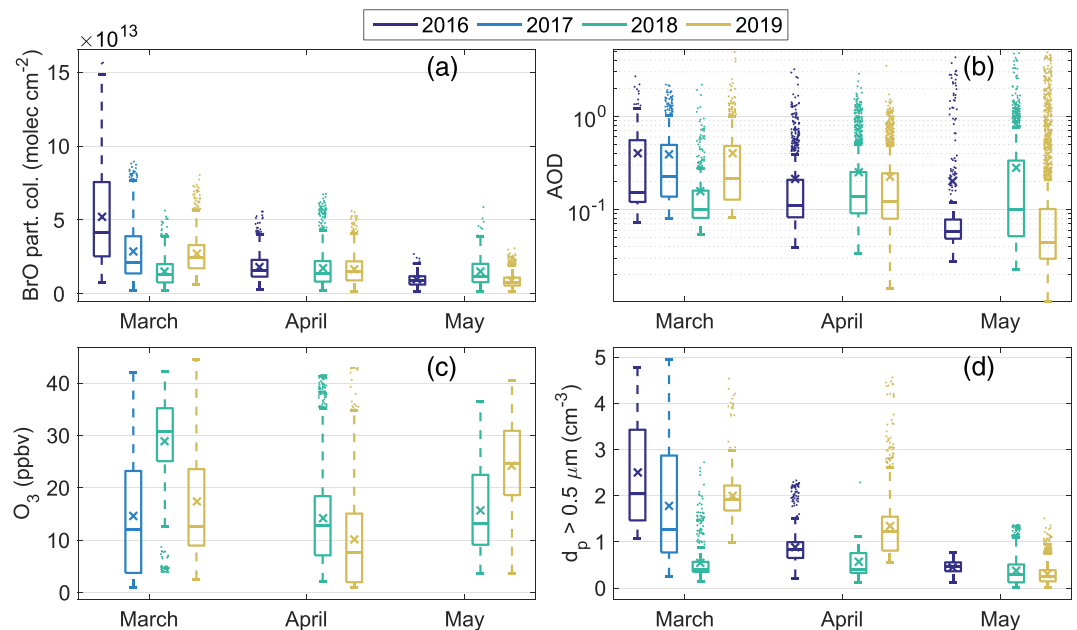


Figure 4. Monthly statistics of (a) 0–4 km MAX-DOAS BrO partial columns, (b) MAX-DOAS AOD, (c) surface ozone measurements at EWS, and (d) in situ measurements of coarse-mode aerosols at the PEARL Ridge Lab. The height of the boxes indicates the 25th and 75th percentiles of the data, with the median marked by the horizontal line, and the mean shown by the x symbols. The whiskers indicate approximately 2.7σ , and the outliers are marked by dots. Note that surface ozone and aerosol measurements were only included for dates when MAX-DOAS data were also available, and there are no MAX-DOAS data for April–May 2017. In addition, no surface ozone measurements are available for 2016.

Ozone measurements (Figure 4c) indicate that more than half of the measurements in March and April (with the exception of March 2018) show at least moderate ODEs (<15 ppbv), and a large fraction of the air samples are strongly depleted in ozone (<10 ppbv; after Halfacre et al., 2014). ODEs are still common in May. During the rest of the year, moderate ODEs occur only in August and September (2% and 0.7% of measurements per month, respectively), and there are only six samples of strongly ozone-depleted air. There are no clear enhancements in the August and September BrO dSCDs, but some BrO might still be present. Excluding March to May data, the overall mean surface ozone concentration measured by the in situ instrument at OPAL is 33 ppbv, with a 7 ppbv standard deviation (2017–2019 data). The mean value for the March to May measurements is 19 ± 12 ppbv.

Variations in surface ozone do not show a clear relationship to BrO columns (Figure 3). This is not surprising since the MAX-DOAS measurements are not sensitive to the surface layers (section 2.3), and some bromine explosions likely terminate before the ozone-depleted air mass arrives in Eureka. Overall, strong and moderate ODEs in the surface ozone data correspond to higher mean and median BrO partial columns than air masses with high surface ozone (Figure S2). The data show large scatter, however, with the largest BrO values observed at similar frequencies for strong ODEs and background ozone conditions. ODEs are often observed in background BrO conditions as well. It has been noted in the literature that the relationship of ozone and BrO is complex even for colocated measurements, due to transport and mixing (e.g., Frieß et al., 2011; Pöhler et al., 2010) and the partitioning of reactive bromine (e.g., Wang et al., 2019).

The AOD values retrieved from MAX-DOAS measurements (Figure 4b) show significant month-to-month and year-to-year variation. While the mean AODs are similar from month to month, the median values and the lowest AOD values show a slight decrease for April and May, when compared to March. Coarse-mode aerosol concentrations (Figure 4d) show a clear decrease from March through May as well. Accumulation-mode aerosol concentrations (not shown), on the other hand, stay relatively constant throughout the spring. The in situ measurements are consistent with the Arctic aerosol cycle (Croft et al., 2016). Ice crystals, common in the spring, also appear less frequently as temperatures increase (EWS observations, not shown). The retrieved AOD likely reflects these variable aerosol conditions, combined with blowing snow events that lead to high AOD values.

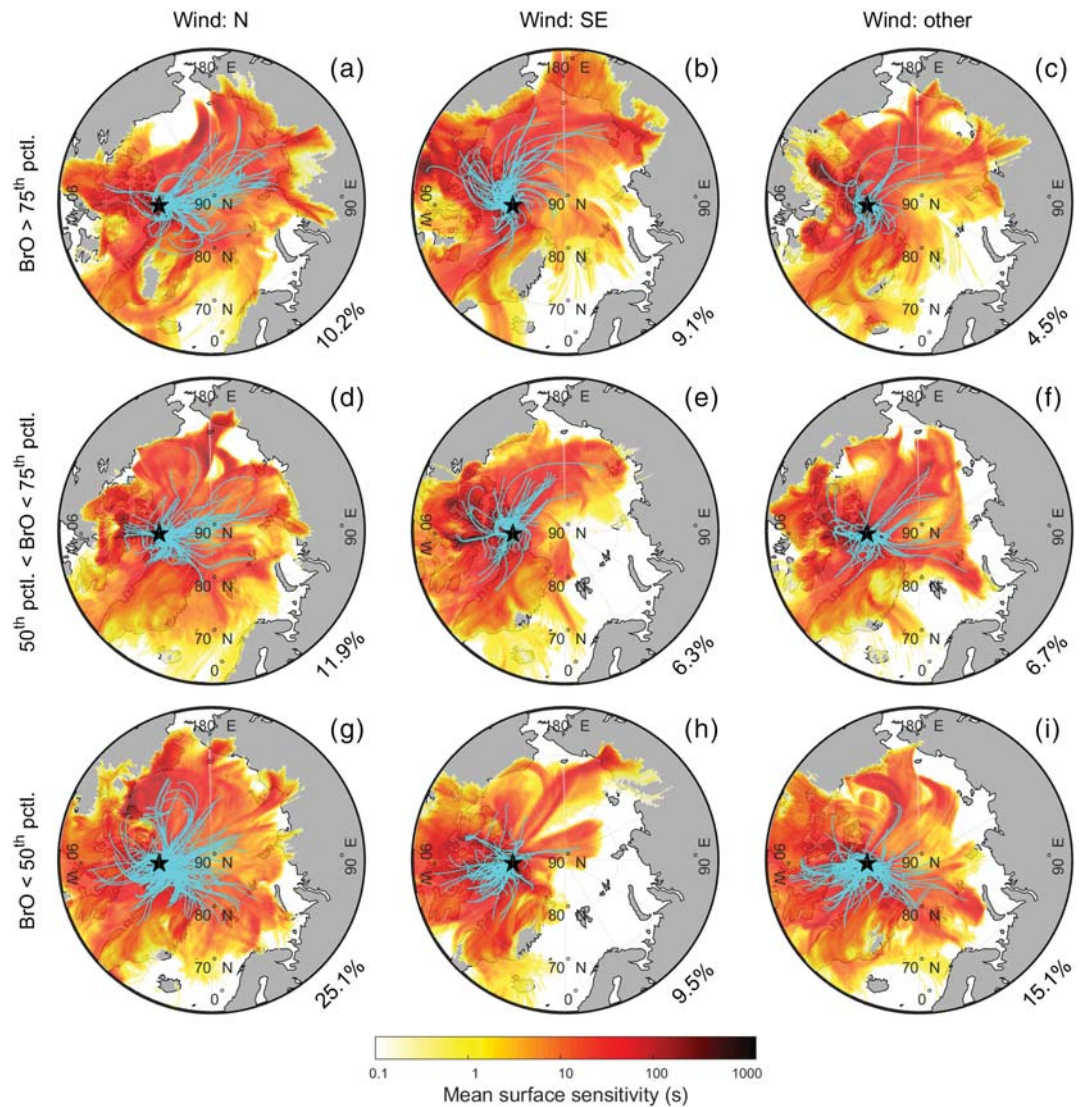


Figure 5. Mean surface sensitivities (log scale color map) and individual trajectories (solid lines) for subsets of the FLEXPART back trajectory data set. The location of Eureka is indicated by the black star. The top row (a–c) shows FLEXPART runs where the corresponding mean BrO was above the 75th percentile of the BrO partial column data set (2.1×10^{13} molec cm^{-2}), the middle row (d–f) shows back trajectories with BrO partial columns between the median (1.3×10^{13} molec cm^{-2}) and the 75th percentile, and the bottom row (g–i) shows FLEXPART runs with BrO below the median. The back trajectories are grouped by local wind direction in each column. The percentages in the bottom right of each map show the portion of back trajectories that fall into the categories defined by the rows and columns. Note that the percentages add up to less than 100% since back trajectories with no wind data were excluded.

3.2. Air Mass History

The next step in characterizing the observed bromine events is understanding the source of the air masses. As discussed in section 2.3, the BrO retrievals are likely not sensitive to the surface layers, and so we expect the observed events to be mostly related to transport. The air mass histories then likely play an important role. Since the wind directions observed at the PEARL Ridge Lab are clearly bimodal (see section 2.1), we might expect to see different air mass histories as a function of local wind direction.

Indeed, FLEXPART back trajectories indicate that the main wind directions correspond to distinct air mass histories. For northerly (N) winds, the majority of air masses arrive at Eureka directly from the Arctic Ocean, and some back trajectories show air mass sources over northern Greenland and the Canadian Arctic Archipelago (Figures 5a, 5d, and 5g). Sensitivity to the surface is weighted toward the Arctic Ocean. For southeasterly (SE) winds, back trajectories are typically “comma-shaped” (indicating the presence of storms

or low-pressure systems) and cluster toward the south and west of Eureka (Figures 5b, 5e, and 5h). The sensitivity is also more heavily weighted toward the Canadian Arctic Archipelago and the western Arctic. Other wind directions correspond to a mix of conditions, with back trajectories mostly from the east of Eureka (Figures 5c, 5f, and 5i). It should be noted that we did not filter the back trajectory data set based on local wind speed, since back trajectory lengths do not correlate well with local winds ($R^2 < 0.1$ for 3-day back trajectories). This indicates that local wind speed is not a good indicator of whether the current air masses are local or transported.

Considering only BrO partial columns of specific magnitudes (from the statistics of the mean BrO partial columns corresponding to each FLEXPART run), the back trajectories differentiate even further. Looking at N winds, BrO partial columns in the top quartile ($> 2.1 \times 10^{13}$ molec cm^{-2}) correspond to reasonably straight back trajectories that connect the central Arctic Ocean to Eureka (Figure 5a). Very few trajectories come from other regions, indicating that contact with sea ice likely plays an important role for N winds. This connection is examined further in section 4.2. When looking at N winds with BrO above the median (1.3×10^{13} molec cm^{-2}) but below the 75th percentile, the back trajectories tell a similar story, but most of them are shorter, originating less than 1,000 km from Eureka (Figure 5d). Finally, BrO events below the median show no clear patterns in the back trajectories for N winds (Figure 5g). This category accounts for one quarter of the entire data set.

For SE winds, the storm-related trajectories discussed earlier correspond mostly to BrO partial columns in the top quartile of the data set (Figure 5b). These storms often originate in the western Arctic and travel over sea ice or over the Canadian Arctic Archipelago. This observation is further supported by the fact that SE winds correspond to a larger fraction of high wind speeds when compared to N winds (Figure 2). BrO events above the median for SE winds show fewer storm-like trajectories, and as for northerly winds, the back trajectories are shorter and indicate more localized influences (Figure 5e). Finally, BrO partial columns below the median show a very different set of air mass histories, with most back trajectories originating from the southeast of Eureka (Figure 5h). From these observations, it appears that storms from the western Arctic almost always bring high BrO concentrations to Eureka (for an exemplary case, see Blechschmidt et al., 2016; Zhao et al., 2016). While a few “comma-shaped” trajectories appear for wind directions other than SE, most of these still correspond to high BrO partial columns. Sections 4.2 and 4.3 shed more light on how storms might contribute to observed BrO enhancements.

4. The Relationship Between BrO and Environmental Variables

From the back trajectory analysis, it is clear that different wind directions correspond to distinct air mass histories. The observed bromine events, then, might also show different characteristics as a function of wind direction. Principal component analysis (PCA, centered and standardized) of the data sets separated by wind direction reveals that the first principal component for N and SE winds accounts for 35% and 38% of the variability in the data sets, respectively. For both wind directions, the first principal component shows that wind speed, sea ice sensitivity, and coarse-mode aerosol concentrations correlate positively with BrO, while temperature is strongly anticorrelated. These relationships are examined in more detail in the following sections. The main difference between the two wind directions according to PCA is the role of atmospheric stability. For N winds, an increase in BrO partial columns is correlated with an increase in the inversion strength between EWS and the PEARL Ridge Lab, while for SE winds, an increase in BrO correlates with a slight decrease in the temperature difference. This is likely related to the impact of storms and corresponding vertical mixing on measurements for SE winds, as discussed below. These results are in agreement with Swanson et al. (2020), who analyzed a multiyear data set of BrO gathered in coastal Alaska (Utqiagvik) and over the Arctic Ocean. Using PCA with a slightly different set of variables, Swanson et al. (2020) identified two distinct meteorological factors associated with BrO enhancements, similar to the factors described above. In our case, both of these factors are associated with BrO enhancements, but their importance varies as a function of wind direction and air mass history. The fact that we observe the statistical signature of strong inversions, which Swanson et al. (2020) associate with surface (0–200 m) BrO enhancements, indicates that transport and topography are likely important factors in our data set, since our partial columns have limited sensitivity to the surface.

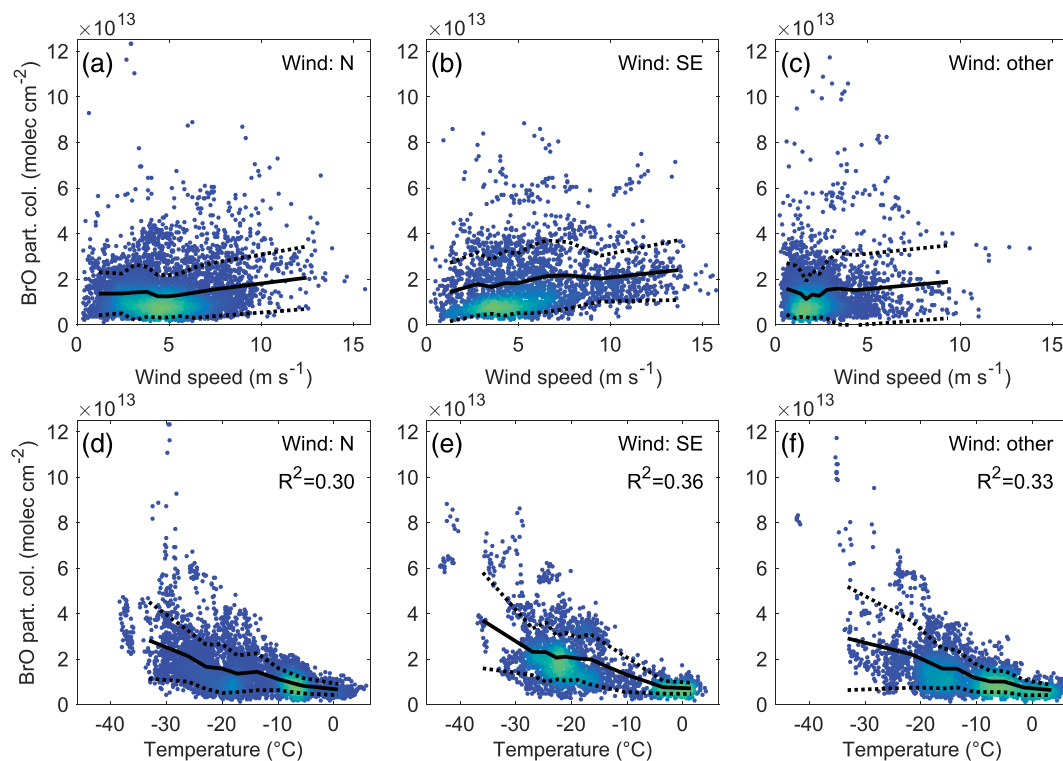


Figure 6. 0–4 km BrO partial columns as a function of (a–c) wind speed and (d–f) temperature. The color scaling shows the normalized density of the points. The solid lines show the mean BrO partial column for each decile of the x-data, and the dotted lines indicate the corresponding one standard deviation. The correlation of BrO with temperature is indicated by the R^2 values in panels (d)–(f).

4.1. Wind Speed, Stability, and Temperature

Wind speed, temperature, and temperature gradients are known to be important factors in bromine chemistry, largely due to their role in determining the vertical structure of BrO (e.g., Peterson et al., 2015). As shown in Figures 6a–6c, the mean BrO partial columns show a slight increase for wind speeds greater than 5 m s^{-1} for N winds and a gradual increase across all wind speeds for SE winds. Other wind directions appear similar to N winds, but there are too few stronger wind events to draw any conclusions. It's important to note, however, that averaging all BrO values might obscure important details. BrO partial columns above the median occur across a range of wind speeds, with no clear pattern. It is the low BrO values that appear to be related to wind speed. For N winds, low BrO events become much less frequent for winds above $7\text{--}8 \text{ m s}^{-1}$, as indicated by the density of the points in Figure 6a. BrO events for SE winds exhibit similar tendencies, and minimum BrO values clearly increase past the same threshold as well (Figure 6b). We argue that these trends are related to vertical mixing, as explained below.

The majority of studies examining the relationship of BrO to wind speed use data from Utqiagvik, Alaska. Frieß et al. (2011) and Liao et al. (2012) found that enhanced surface BrO corresponded to episodes of high winds ($>5\text{--}6 \text{ m s}^{-1}$) and increased surface extinction. Peterson et al. (2015), however, found that 0–2 km BrO partial columns showed no clear dependence on wind speed. This is consistent with our observations for BrO partial columns above the median. Peterson et al. (2015) also noted that wind speeds above 8 m s^{-1} almost always led to vertically distributed BrO events and larger column values, which likely explains why we observe an increase in the minimum BrO values past a similar threshold. Since our retrievals are likely only sensitive to BrO aloft, we expect to see little to no BrO for shallow boundary layer events and high BrO for distributed events. If weaker winds correspond to a mix of shallow and distributed events, the retrieved BrO partial columns might show a wide range of values, while wind speeds above $7\text{--}8 \text{ m s}^{-1}$ would result in larger BrO partial columns only.

The influence of strong winds and vertical mixing highlights the potential impact of atmospheric stability on the BrO partial columns. Here we use the temperature difference between EWS and the PEARL Ridge

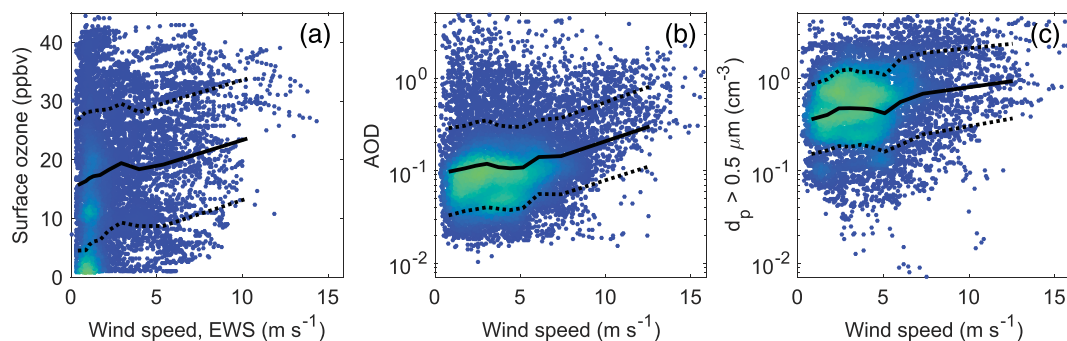


Figure 7. (a) Surface ozone concentrations as a function of wind speed measured at EWS, alongside (b) MAX-DOAS AOD and (c) coarse-mode aerosol concentrations as a function of wind speed measured in the PEARL Ridge Lab. The color scaling shows the normalized density of the points. The solid lines show the mean BrO partial column for each decile of the x-data, and the dotted lines indicate the corresponding one standard deviation. Note that the aerosol concentrations are plotted on a logarithmic scale to highlight the change in the minimum values.

Lab (ΔT_{610m}), calculated from radiosonde measurements, as a measure of atmospheric stability. Wind speed and ΔT_{610m} do not show a clear relationship. While near-zero ΔT_{610m} are more frequent for strong winds (above 7–8 $m s^{-1}$), the inversion strength is largely independent of wind speed for weaker winds.

When a temperature inversion is present between EWS and the PEARL Ridge Lab, the inversion strength appears to have little influence on the BrO partial columns. BrO values above the 90th percentile peak at inversion strengths of approximately 10°C for N winds and around 0°C for SE and other wind directions, although these peaks reflect the most frequent ΔT_{610m} values for each wind direction. BrO values below the 90th percentile are observed across a wide range of ΔT_{610m} values (from $-4^{\circ}C$ to $20^{\circ}C$), with a decline in the maximum BrO only past $\Delta T_{610m} = 15^{\circ}C$. This indicates that BrO aloft is often decoupled from the surface in Eureka, since the atmosphere is expected to be stably stratified for strong inversions, and our measurements are likely not sensitive to BrO in the surface layer. These results contrast with Peterson et al. (2015), who found that stronger inversions lead to higher near-surface BrO concentrations and reduced column amounts. We do observe large BrO partial columns during strong inversions, and so these events might be related to long-range transport or to local activation of bromine on aerosol particles (examined in more detail in section 4.3). An important caveat is the unknown effect of topography on the measurements presented here: Utqiagvik is located on flat terrain, while the PEARL Ridge Lab is surrounded by ridges and valleys. Winds blowing over ridges could potentially inject “surface” air into layers hundreds of meters above the open fjords. In addition, the MAX-DOAS instrument is looking down a valley (Figure 1, section 2.3), and so the low elevation angle light paths are always closer to the surface than the retrieval algorithm assumes. Surface air masses could therefore still influence the BrO concentrations even when strong inversions are present.

While low wind speeds or atmospheric stability do not have a clear direct influence on BrO partial columns, the mean surface ozone values from EWS show an increase with wind speed for very weak winds (colocated wind data from EWS, Figure 7a) and a decrease with increasing ΔT_{610m} (not shown). Samples strongly depleted in ozone are observed most often for wind speeds below 2 $m s^{-1}$. These events correspond to a wide range of temperature inversion strengths (mean $\Delta T_{610m} = 6.9 \pm 4.5^{\circ}C$) and BrO partial column values, which is likely related to the fact that, due to the effects of topography, calm conditions at EWS do not necessarily correspond to calm weather at the PEARL Ridge Lab. Only events with complete depletion of surface ozone (concentrations below 2 ppbv) occur preferentially during strong inversions (mean $\Delta T_{610m} = 8.0 \pm 3.5^{\circ}C$), possibly representing local bromine release from the snowpack. This is in agreement with Helmig et al. (2012), who found that ODEs in Utqiagvik occurred primarily in calm conditions, and Halfacre et al. (2014), who came to the same conclusion using measurements from buoys across the Arctic Ocean.

Strong winds, on the other hand, represent a different regime. Helmig et al. (2012) argued that the increased mixing by stronger winds might replenish ozone fast enough to counteract any potential increase in bromine concentrations. As shown in Figure 7a, minimum hourly ozone concentrations show a clear increase for wind speeds greater than approximately 5 $m s^{-1}$, and ODEs become increasingly rare as wind speeds

increase. As described above, stronger winds are more likely to coincide with near-zero ΔT_{610m} values (signifying a deeper boundary layer), as well as increasing BrO partial columns (Figures 6a–6c). We take strong SE winds as an example: When EWS wind speeds are greater than 8 m s^{-1} , 85% of the BrO partial columns are above the overall median of the BrO data set. SE winds are commonly associated with storms and good mixing, and the largest BrO partial columns are observed for surface ozone concentrations of $\sim 30 \text{ ppbv}$ (see also Figure S2). In fact, for SE winds with EWS wind speeds greater than 8 m s^{-1} , surface ozone concentrations generally increase with BrO values, with a corresponding R^2 value of 0.25. These results indicate that for strong winds, mixing of ozone-rich air from above is sufficient to maintain background ozone concentrations even in high BrO conditions. The observation that BrO partial columns are apparently not diluted by the same mixing that replenishes ozone indicates that BrO is either continuously mixed up from the snowpack or that recycling and/or release from aerosol particles is more efficient in strong winds.

It is known that bromine release occurs predominantly at lower temperatures (e.g., Burd et al., 2017). BrO partial columns show a clear decrease as temperature increases, as seen in Figures 6d–6f. The relationship is not linear, but R^2 values indicate that temperature (at 610 m) alone can explain a third of the variance in the BrO data set, independent of wind direction. Minimum BrO partial columns also show an upward trend with decreasing temperatures below approximately -25°C , likely related to the fact that very cold weather at the PEARL Ridge Lab (which is usually above the inversion layer) often corresponds to strong winds, weak inversions, and good mixing. When considering the temperatures at EWS, this feature disappears. The strong downward trend of the maximum BrO with temperature, however, is present regardless of the altitude of the temperature measurements. We observe enhanced BrO up to temperatures just below freezing, and the partial columns decrease to near the approximate detection limit for temperatures around or above 0°C . The largest BrO partial columns are observed at temperatures below -10°C .

Tarasick and Bottenheim (2002) argued, based on ozonesonde measurements, that ODEs require temperatures below -20°C . More recent studies, however, observed ODEs at temperatures well above this threshold (Bottenheim et al., 2009; Halfacre et al., 2014; Jacobi et al., 2010). Jacobi et al. (2010) and Halfacre et al. (2014) both argued that the relationship of ozone and temperature needs to be interpreted with caution due to the role of transport in determining local ozone levels. Our results are consistent with Burd et al. (2017), who reported enhancements of 1° elevation BrO dSCDs up to, but not above, freezing temperatures in Utqiagvik, Alaska. The authors noted that peak dSCDs increased from 0 to -10°C , and dSCDs showed a relatively flat envelope below -10°C . Using partial columns from a subset of the same data set, Peterson et al. (2015) found no clear relationship between BrO and temperature. That data set, however, only included measurements up to -5°C , and so the results are not inconsistent with Burd et al. (2017) and the present study. Using long-path DOAS measurements in the Amundsen Gulf, Pöhler et al. (2010) observed a similarly strong negative trend in the maximum near-surface BrO but sloping to a high threshold of -15°C (the highest observed temperature) instead of 0°C . It should be noted, however, that those measurements did not extend into May and thus did not experience the higher temperatures associated with the end of the bromine activation season.

4.2. Relationship to Sea Ice Sensitivity

If the lofted BrO we observe is related to transport, we might expect to see a correlation with time spent in areas covered by sea ice, as snow over FYI is commonly considered a major source of bromine to the atmosphere (e.g., Peterson et al., 2016). Maps of the distribution of FYI and MYI for the measurement period in each year are shown in Figure S3. In our data set, BrO shows a clear relationship to FYI sensitivity for N winds only (Figure 8a). The maximum BrO partial columns increase with increasing FYI sensitivity, and the mean BrO partial columns show an increase as well. For N winds, air masses with enhanced BrO mostly come from over the Arctic Ocean (Figure 5), and so they likely transport bromine that was released from the snow over the sea ice. The lack of local influences is further supported by the fact that the largest BrO partial columns were observed when strong temperature inversions were also present (section 4.1).

For SE and other wind directions, the largest BrO partial columns still tend to coincide with high FYI sensitivity, but the mean BrO values are largely independent of time spent in FYI areas (Figures 8b and 8c). Since for SE winds, BrO events above the median often correspond to storms, this indicates that the snowpack over FYI is likely not the only source of storm-related BrO. Enhanced BrO events coincided with air masses that originated in a variety of regions, including over the Canadian Arctic Archipelago, where the inland snowpack might play a larger role than FYI (Peterson et al., 2018). The role of local BrO sources (snowpack

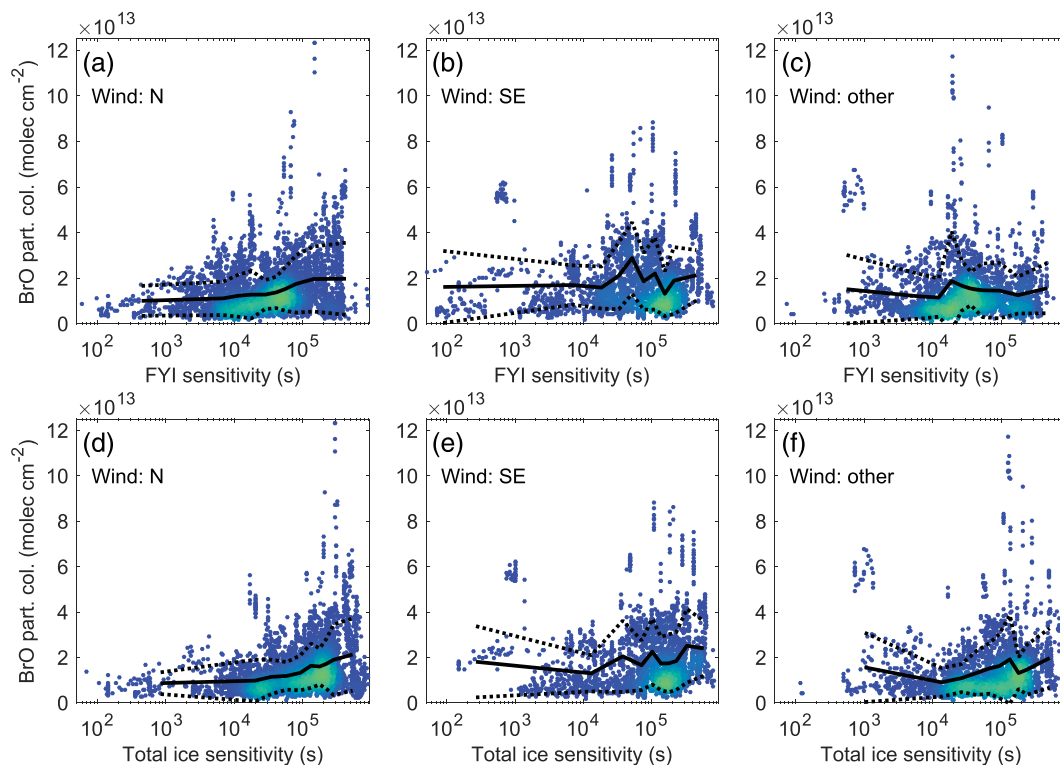


Figure 8. 0–4 km BrO partial columns as a function of (a–c) FYI sensitivity and (d–f) all sea ice sensitivity. The color scaling shows the normalized density of the points. The solid lines show the mean BrO partial column for each decile of the sensitivity data, and the dotted lines indicate the corresponding one standard deviation.

and locally generated aerosol) might also be important. For other wind directions, we did not expect a close relationship to FYI sensitivity, as most back trajectories originated to the south or east of Eureka.

Good correlation between air mass contact with FYI and measured BrO has been reported by several studies (Nghiem et al., 2012; Peterson et al., 2016; Simpson et al., 2007). Frieß et al. (2011), however, found that time spent in FYI areas was not in itself a good predictor of BrO concentrations. The authors noted that simple characterizations might not be sufficient to capture the complex influences of air mass history, meteorology, and microphysical parameters. Our approach still utilizes a relatively simple parametrization, and it is evident that FYI sensitivity alone does not explain the local BrO variability. The different impact of FYI sensitivity as a function of wind direction highlights the importance of meteorology at sites that experience distinct weather regimes. Furthermore, FYI is not necessarily the best metric to compare to BrO measurements in Eureka.

When considering all sea ice sensitivity (FYI and MYI, Figures 8d–8f), the relationship to the highest BrO values is similar to the FYI case discussed above. The mean BrO partial columns, however, now show at least a modest increase as a function of sea ice sensitivity for all wind directions. While our sea ice sensitivity metric is only weakly correlated to BrO, we can use correlation coefficients (R) as a more tangible measure of the changes in the relationship. R values improve from 0.28, 0.07, and -0.01 (for N, SE, and other wind directions, respectively) to 0.32, 0.11, and 0.09 when all sea ice is considered. It appears that considering FYI and MYI together is a slightly better indicator of bromine activation than FYI sensitivity only. Extending the back trajectory durations to 5 days (instead of 3 days) does not change the results. Compared to other sites, sensitivity to MYI might be more prominent in Eureka, since the Arctic Ocean off the coast of Ellesmere Island is usually covered by perennial ice. It should be noted that the observed sensitivity to different sea ice areas is not independent. The maximum MYI sensitivity values increase with FYI sensitivity, although low MYI sensitivity values occur across a wide range of FYI sensitivity values. Even so, it is possible that new snow on MYI also contributes to bromine release.

Seasonal ice (FYI) contributes to the snow salinity required for bromine release via upward migration of brine into the snowpack, through the influence of frost flowers, and via atmospheric processes such as sea spray SSA from leads and polynyas (e.g., Domine et al., 2004; Frey et al., 2020; Hara et al., 2017). On the other hand, sea ice that survives the summer (MYI) has much lower salinity, and MYI areas are more consolidated, with fewer areas of open water. As a result, snow on FYI is commonly considered a much more likely source of bromine than MYI. Atmospheric processes, however, might still create favorable conditions for bromine release on MYI. Arctic haze (pollution transported from northern Eurasia) is ubiquitous over the Arctic Ocean in the winter and spring. The haze consists of aged and acidic accumulation-mode (approximately $0.1 \mu\text{m} < d_p < 0.5 \mu\text{m}$) particles, composed mainly of sulfate, black carbon, and sea salt (e.g., Croft et al., 2016; Quinn et al., 2007). Haze aerosols are deposited onto the surface of the snowpack and can be scavenged by falling and blowing snow as well (e.g., Nawrot et al., 2016; Sharp et al., 2002). It has been shown that acidity and markers of halogen activation (Br^- , Hg) in the snowpack correlate with exposure to Arctic haze (Douglas & Sturm, 2004; Nawrot et al., 2016; Toom-Sauntry & Barrie, 2002). While this process impacts snow on all sea ice, as well as snow on land, the additional bromine source from MYI areas might be detectable at sites like Eureka, situated near the perennially ice-covered regions of the Arctic Ocean.

Identifying the source regions of transported BrO events is challenging, and it is outside the scope of this project. Using 3-day back trajectories, there are several enhanced BrO events with high MYI to all sea ice sensitivity ratios (4% of the data set has a ratio of 0.9 or greater), but even the small fraction of FYI sensitivity is always sufficient to explain the observed BrO. For example, most of these events correspond to easily identifiable BrO plumes that originate over FYI in the western Arctic (data from the University of Bremen GOME-2 data browser, https://www.iup.uni-bremen.de/doas/scia_data_browser.htm). The most probable case for MYI bromine release is a single event (16 May 2019) that maintains the 90% MYI sensitivity even when the back trajectories are extended to 5 days. BrO concentrations on May 16 were in the top quartile of the May 2019 BrO measurements ($\sim 1.6 \times 10^{13}$ molec cm^{-2} ; see Figure 4), and surface ozone was in the 15–20 ppbv range. The corresponding back trajectories indicate that the mean mixing layer height for all particles was less than 280 m during the 5-day FLEXPART runs. This is below the mean and median mixing layer height for all FLEXPART runs, indicating fairly calm conditions along the back trajectories, ideal for snowpack bromine release. The timing of this event might also play a role. The influence of Arctic haze (as well as bromine plumes that pass over MYI) would accumulate during the course of the spring, and the potentially increasing salinity and bromide content (Douglas & Sturm, 2004; Toom-Sauntry & Barrie, 2002) of snow over MYI could create favorable conditions for bromine release in May.

Previous studies have noted the potential role of MYI in bromine chemistry. Peterson et al. (2016) found that time spent in all ice areas correlated slightly better with BrO than FYI contact only, and the authors reported *R* values similar to those seen in this study for N winds. Gilman et al. (2010) came to similar conclusions using ozone as a tracer for the presence of halogens. The authors of both studies noted, however, that all ice contact is highly correlated with FYI contact. More recently, Peterson et al. (2019) analyzed bulk snow samples collected over FYI and MYI in the central Arctic and found that surface snow over MYI was frequently depleted in bromide, indicating that MYI acts as a source of bromine to the atmosphere. Based on snowpack salinity and depth measurements, the authors concluded that atmospheric processes, as opposed to upward migration of brine, are likely the key factors in determining halogen concentrations in surface snow. In addition to direct bromine release, the snowpack on sea ice is also a source of blowing snow, which then may generate SSA particles (Frey et al., 2020; Giordano et al., 2018; Huang et al., 2018). While investigating the role of SSA in bromine release, Choi et al. (2018) found that bromine explosion frequency correlated better with modeled SSA emission flux over all sea ice than with SSA emissions over FYI only (although given the results of Peterson et al., 2019, SSA from snow on MYI might not be an ideal source of bromine). These results lend support to the idea that bromine chemistry is active in MYI areas. Determining the exact contribution of MYI (either through the snowpack or via SSA production) requires further research.

4.3. The Role of Aerosol Particles

Transport of BrO over long distances by storms (Begoin et al., 2010; Blechschmidt et al., 2016; Sihler et al., 2012; Zhao et al., 2016) indicates that aerosols are important for recycling and maintaining lofted BrO concentrations. As discussed in section 3.2, SE winds often correspond to storms passing over Eureka, and these air masses show little correlation between sea ice sensitivity and BrO partial columns (section 4.2). Aerosols might then be the key for the large BrO partial columns we observe. Furthermore, since the BrO

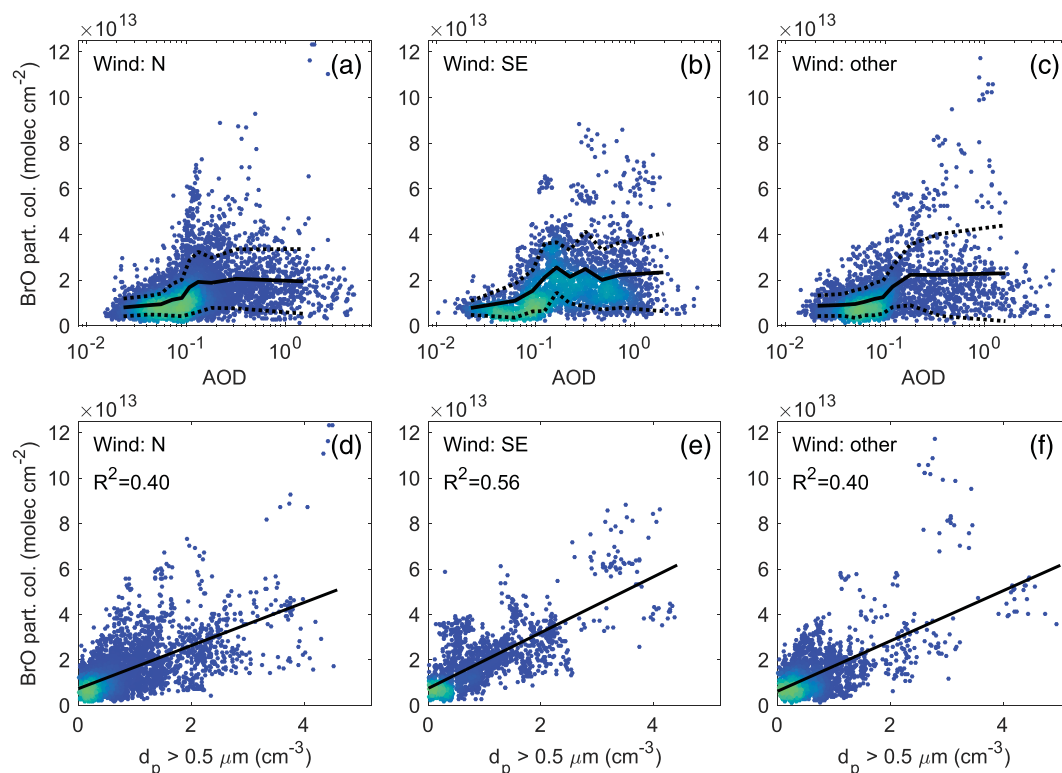


Figure 9. 0–4 km BrO partial columns as a function of (a–c) retrieved AOD and (d–f) coarse-mode aerosol number concentrations. The color scaling shows the normalized density of the points. For panels (a)–(c), the solid lines show the mean BrO partial column for each decile of the x-data, and the dotted lines indicate the corresponding one standard deviation. For panels (d)–(f), the solid lines show the linear least squares fit, with the R^2 values indicated on the plots.

partial columns presented here have limited sensitivity to local snowpack sources, we expect aerosols to play an important role regardless of wind direction.

The mean BrO partial columns show a clear increase with increasing AOD values (Figures 9a–9c). As anticipated, this increase is most pronounced for SE winds, and this wind direction sees the largest ratio of high to low AOD observations as well. 70% of AODs are above 0.1 for SE winds, while the same statistic is 45% for N and other wind directions. High AOD values don't necessarily correspond to large BrO partial columns, but the largest BrO partial columns are observed for $AOD > 0.1$, and mean BrO remains high past this value as well. Frieß et al. (2011), Peterson et al. (2015), Simpson et al. (2017), and Swanson et al. (2020) all found that increasing extinction and high AOD corresponded to larger BrO values. Simpson et al. (2017) concluded that high extinction was necessary, but not sufficient, for BrO layers to migrate aloft, in agreement with the results presented here. The aerosol extinction retrieval, however, does not separate the sources of extinction (aerosols, ice crystals, and blowing snow). In our data set, high AOD corresponds to a wide range of aerosol concentrations (for both accumulation and coarse modes). In situ aerosol measurements, therefore, might be a more appropriate base of comparison.

Indeed, BrO values show good correlation to coarse mode aerosol concentrations ($>0.5 \mu\text{m}$, Figures 9d–9f). The relationship is approximately linear, with the highest R^2 value for SE winds (0.56) and lower R^2 values (0.4) for other wind directions. Both minimum and maximum BrO values show a linear increase with increasing coarse-mode aerosol concentrations, and this envelope is the tightest for SE winds. Interestingly, accumulation-mode aerosols ($0.1\text{--}0.5 \mu\text{m}$; Figure S4) are not at all correlated to BrO partial columns ($R^2 \approx 0$). From our data set, it appears that coarse-mode aerosols play a crucial role in bromine chemistry, and the presence of these aerosols is a necessary and sufficient condition for observing high BrO values at our elevated measurement site.

These results are in good agreement with Peterson et al. (2017), who observed a BrO plume sustained on, and transported with, a layer of supermicron aerosol particles. The authors also noted that submicron aerosol

particles were likely not a controlling factor in BrO recycling. While we use 0.5 μm instead of 1 μm as the diameter cutoff, our conclusions do not change if we follow Peterson et al. (2017) and use supermicron particles. We find that aerosols larger than 0.5 μm correlate better with BrO (R^2 values improve by 8% and 40% for N and SE winds, respectively). In situ measurements support the role of aerosols in bromine chemistry. Hara et al. (2002) found that aerosol particles larger than 2 μm were generally depleted in Br^- . In Antarctica, Legrand et al. (2016) observed Br^- depletion in coarse-mode aerosols in the spring and Br^- enhancement in accumulation-mode particles. These conclusions were supported by the results of Giordano et al. (2018) as well. Hara et al. (2018), however, found that Br^- was depleted in all aerosols, regardless of size. Frey et al. (2020) came to similar conclusions, although they only measured aerosols with $d_p > 0.36 \mu\text{m}$.

There are no composition measurements available for springtime aerosol in Eureka for 2016–2019. The limited number of coarse-mode aerosol sources in the Arctic spring implies that we most likely observe SSA, which might be generated by blowing snow (Frey et al., 2020; Giordano et al., 2018; Huang et al., 2018; Zhao et al., 2017) or released from leads in the sea ice (Kirpes et al., 2019; Leck et al., 2002; May et al., 2016; Nilsson et al., 2001). SSA generated from local blowing snow would correspond to high aerosol load for wind speeds above the blowing snow threshold. Figures 7b and 7c show that both minimum AOD values and minimum coarse-mode aerosol concentrations clearly increase with wind speed for strong winds. Using a simple temperature-dependent model (after Li & Pomeroy, 1997; see Text S2), the mean wind speed threshold for blowing snow was estimated to be between 7 and 8 m s^{-1} , in line with commonly accepted values (Frey et al., 2020; Giordano et al., 2018; Li & Pomeroy, 1997). Considering data with wind speeds below the threshold (from coincident temperature measurements), coarse-mode aerosol concentrations are $0.68 \pm 0.65 \text{ cm}^{-3}$ (mean and standard deviation). For wind speeds above the threshold, the mean value is $1.32 \pm 0.98 \text{ cm}^{-3}$, indicating that we measure significantly higher coarse-mode aerosol load ($p < 0.001$) for wind speeds above the blowing snow threshold. High aerosol concentrations, on the other hand, occur over a range of wind speeds, with only a slight preference for stronger winds. This indicates that most of the aerosol we observe is likely not produced locally, but transported to the measurement location. The increased aerosol load for strong winds is also consistent with the threshold for lead-based SSA production ($4\text{--}5 \text{ m s}^{-1}$; e.g., May et al., 2016; Leck et al., 2002), although local wind speed is not necessarily representative of wind speed along the back trajectories. To investigate the potential contribution of leads-sourced SSA to the measurements, we used MODIS/Aqua and MODIS/Terra L3 daily sea ice data (Hall & Riggs, 2015a, 2015b) to examine sea ice coverage near Eureka. The sea ice maps indicate that during the study period, there were no clearly identifiable leads or areas of open water within 600–800 km to the north and west of Eureka, where most of the air masses pass through (section 3.2). However, cloud cover often obscures much of the sea ice near Eureka, and so the presence of leads cannot be ruled out. Leads further along the back trajectories (e.g., in the western Arctic, where the storms we observe typically originate) likely also contribute to the aerosol concentrations measured in Eureka. A potential nearby source of lead-sourced SSA is northern Baffin Bay, which often contains polynyas as early as March and becomes largely ice-free by early May. Back trajectories, however, show little sensitivity to this area, especially when BrO concentrations are high. Overall, our measurements are consistent with the possibility that some SSA is produced locally from blowing snow. The proportion and sources of transported aerosols, however, cannot be determined based on the data used in this study.

Accumulation-mode aerosols are likely dominated by the Arctic haze (section 4.2), with some potential contribution from SSA. Frey et al. (2020) noted that less saline blowing snow would create smaller particles, potentially as small as d_p on the order of 1 nm. To separate the impact of the Arctic haze, we compared BrO partial columns to black carbon concentrations (another haze tracer) from Photoacoustic Extinction measurements at the PEARL Ridge Lab (Vicente-Luis et al., 2020). The results (Figure S4) indicate a similar lack of correlation as seen in the accumulation-mode comparisons, suggesting that Arctic haze does not play a direct role in bromine activation in Eureka. It is possible, however, that these particles participate in bromine recycling once BrO is already present, as haze aerosols are composed partly of sea salt (e.g., Croft et al., 2016; Quinn et al., 2007).

It is still unclear to what extent SSA contributes to direct bromine release, as opposed to recycling of bromine released elsewhere. The recent results of Legrand et al. (2016) and Hara et al. (2018) indicate that SSA is a major source of tropospheric bromine in Antarctica. Frey et al. (2020) came to the same conclusion and showed that bromine release from SSA took place between 2 and 29 m above the sea ice surface. While these results can likely be generalized to all polar regions, similar measurements are needed in the Arctic

to confirm the role of SSA. Satellite measurements of BrO by Choi et al. (2018) showed good correlation to simulated SSA emission flux in the Arctic and no correlation to FYI areas, indicating that SSA is responsible for at least part of the bromine release in the Arctic. The very good correlation between coarse-mode aerosols and BrO observed in this study supports this conclusion. Given that the coarse-mode aerosols we observe are most likely SSA and the observation that high coarse-mode aerosol concentrations always correspond to high BrO values, these results strongly suggest that coarse-mode aerosols play an active role in bromine release at Eureka.

5. Conclusions

We have presented 0–4 km BrO partial columns from four bromine activation seasons at an elevated measurement site in Eureka, Canada. We have found that local wind directions show two distinct modes (N and SE) and that the observed BrO events show different characteristics for each of these wind directions. Air mass histories for enhanced BrO events (inferred from FLEXPART back trajectory simulations) show two modes as well: N winds transport air masses from over the Arctic Ocean, while SE winds generally correspond to storms that originate in the western Arctic or over the Canadian Arctic Archipelago.

We have observed BrO at temperatures up to 0°C. It appears that temperature alone accounts for a third of the variance in the BrO data set, and maximum BrO values increase almost linearly with decreasing temperatures. We have found that, due to the elevation of the measurement site (610 m), the retrieved BrO partial columns are likely not sensitive to the surface (sea level), and the MAX-DOAS instrument measures above the boundary layer most of the time. As a result, the strength of the temperature inversion has a limited impact on the BrO values presented here, since we do not observe the shallow bromine events that typically show a strong dependence on atmospheric stability. When the boundary layer is deep, however, the effects of the enhanced vertical mixing manifest as an increase in the minimum BrO values for wind speeds of 7–8 m s⁻¹ or greater. Minimum surface ozone concentrations increase even in moderate wind speeds, and ODEs become less and less frequent as wind speeds increase past 7–8 m s⁻¹. While these high-wind events most often correspond to enhanced BrO, mixing of ozone-rich air from higher altitudes is sufficient to counteract ozone destruction.

We have shown that while air masses have similar sensitivity to FYI areas regardless of wind direction, BrO partial columns increase with FYI sensitivity for N winds only. On the other hand, when all sea ice sensitivity (FYI + MYI) is considered, the relationship to BrO improves for all wind directions. Snow on MYI is often neglected as a source of bromine, due to its lower salinity compared to FYI. It is possible, however, that atmospheric processes (e.g., exposure to Arctic haze) could create favorable conditions for bromine release from snow on MYI.

Since the BrO we observe at Eureka is likely often decoupled from the surface, high aerosol load (as indicated by the retrieved AOD values) was necessary to maintain high BrO concentrations. We have examined the contribution of accumulation-mode (0.1–0.5 μm) and coarse-mode (>0.5 μm) aerosols using in situ measurements. The accumulation mode is likely dominated by the Arctic haze, and these particles show no direct relationship to BrO. The presence of coarse-mode aerosols, however, was a necessary and sufficient condition for observing large BrO partial columns with an instrument located above the boundary layer. It is most likely that these particles are SSA. The strongest correlation ($R^2 = 0.56$) was observed for SE winds that often correspond to storms and favorable conditions for both transport and local production of SSA. The good correlation between BrO and coarse-mode aerosols supports the view that SSA is a direct source of bromine to the polar troposphere. More measurements of the composition and vertical distribution of aerosols would be required to quantify the contribution of SSA to the Arctic halogen budget.

From the measurements presented here, it appears that BrO above the boundary layer is common in Eureka from March to May. The role of mountainous terrain on boundary layer dynamics, however, needs to be quantified. The exact influence of near-surface air on our measurements is unclear, and it is possible that BrO aloft is never fully decoupled from the surface. Much of the Canadian Arctic is covered by similar topography, and so a better understanding of the mechanisms behind the vertical distribution of bromine is important for reconciling the differences between ground-based and satellite observations, as well as addressing the issues of tropospheric ozone depletion and mercury deposition in a rapidly changing Arctic.

Data Availability Statement

The BrO partial columns and AOD values (alongside the retrieved profiles, AVKs, and DOFS), the paired weather station data from the PEARL Ridge Lab, and paired accumulation and the coarse-mode aerosol data are available on the Scholars Portal Dataverse (Bognar et al., 2020). Ozone sonde measurements are available on the World Ozone and Ultraviolet Radiation Data Centre (<https://woudc.org/data/explore.php?lang=en>, Station: Eureka (315), Instrument: Ecc). Radiosonde data are available through the University of Wyoming Upper Air Database (<https://weather.uwyo.edu/upperair/sounding.html>, Station Number: 71917). EWS weather records can be found on the ECCC historical weather database (https://climate.weather.gc.ca/historical_data/search_historic_data_e.html, Search by Station Name: Eureka A). Surface ozone measurements are available on the National Centers for Environmental Information database at NOAA (McClure-Begley et al., 2014). EASE-Grid sea ice age data (Tschudi et al., 2019) and MODIS sea ice coverage (Hall & Riggs, 2015a, 2015b) are available on the National Snow and Ice Data Center at NASA (see DOI for each data set under the relevant reference). We used FLEXPART version 10.1beta. The code is available at <https://www.flexpart.eu/wiki/FpRoadmap>, and the reanalysis data used for the back trajectory calculations (Saha et al., 2011) are available at <https://rda.ucar.edu/datasets/ds094.0/>. We used subsets with the “FLEXPART Model Input: 6-hour Forecasts” parameter preset. The HEIPRO retrieval algorithm is described in Frieß et al. (2011) and Yilmaz (2012). We used version 1.2, alongside SCIATRAN version 2.2 (available at <https://www.iup.uni-bremen.de/sciattran/download/index.html>; Rozanov et al., 2005).

Acknowledgments

The 2016–2019 PEARL-GBS, OPC, APS, and SMPS measurements were made at PEARL by CANDAC. CANDAC (led by James R. Drummond) has been supported by the Atlantic Innovation Fund/Nova Scotia Research Innovation Trust, Canada Foundation for Innovation, Canadian Foundation for Climate and Atmospheric Sciences (CFCAS), Canadian Space Agency (CSA), Environment and Climate Change Canada (ECCC), Government of Canada International Polar Year funding, Natural Sciences and Engineering Research Council (NSERC), Northern Scientific Training Program (NSTP), Ontario Innovation Trust, Polar Continental Shelf Program, and Ontario Research Fund. The PEARL-GBS, OPC, APS, SMPS, and ozonesonde measurements were also supported by the Canadian Arctic ACE/OSIRIS Validation Campaigns (led by Kaley A. Walker), which were funded by CSA, NSERC, NSTP, and ECCC. K. Bognar was partially supported by the NSERC CREATE Training Program in Arctic Atmospheric Science, and the Arctic Validation And Training for Atmospheric Research in Space program, funded by CSA. The authors wish to thank PEARL Site Manager Pierre Fogal, the CANDAC operators, and the staff at ECCC's Eureka Weather Station for their contributions to data acquisition, and logistical and on-site support.

References

Abbatt, J. P. D., Thomas, J. L., Abrahamsson, K., Boxe, C., Granfors, A., Jones, A. E., et al. (2012). Halogen activation via interactions with environmental ice and snow in the polar lower troposphere and other regions. *Atmospheric Chemistry and Physics*, *12*(14), 6237–6271. <https://doi.org/10.5194/acp-12-6237-2012>

Barrie, L. A., Bottenheim, J. W., Schnell, R. C., Crutzen, P. J., & Rasmussen, R. A. (1988). Ozone destruction and photochemical reactions at polar sunrise in the lower Arctic atmosphere. *Nature*, *334*(6178), 138–141. <https://doi.org/10.1038/334138a0>

Begoin, M., Richter, A., Weber, M., Kaleschke, L., Tian-Kunze, X., Stohl, A., et al. (2010). Satellite observations of long range transport of a large BrO plume in the Arctic. *Atmospheric Chemistry and Physics*, *10*(14), 6515–6526. <https://doi.org/10.5194/acp-10-6515-2010>

Berg, T., Pfaffhuber, K. A., Cole, A. S., Engelsen, O., & Steffen, A. (2013). Ten-year trends in atmospheric mercury concentrations, meteorological effects and climate variables at Zeppelin, Ny-Ålesund. *Atmospheric Chemistry and Physics*, *13*(13), 6575–6586. <https://doi.org/10.5194/acp-13-6575-2013>

Blechschmidt, A.-M., Richter, A., Burrows, J. P., Kaleschke, L., Strong, K., Theys, N., et al. (2016). An exemplary case of a bromine explosion event linked to cyclone development in the Arctic. *Atmospheric Chemistry and Physics*, *16*(3), 1773–1788. <https://doi.org/10.5194/acp-16-1773-2016>

Bognar, K., Strong, K., Chang, R. Y.-W., Fogal, P., & Hayes, P. L. (2020). Profiles of BrO and aerosol retrieved from PEARL-GBS MAX-DOAS measurements at Eureka, Canada. <https://doi.org/10.5683/SP2/GJENGJ>

Bottenheim, J. W., Gallant, A. G., & Brice, K. A. (1986). Measurements of NO_y species and O₃ at 82°N latitude. *Geophysical Research Letters*, *13*(2), 113–116. <https://doi.org/10.1029/GL013i002p00113>

Bottenheim, J. W., Netcheva, S., Morin, S., & Nghiem, S. V. (2009). Ozone in the boundary layer air over the Arctic Ocean: Measurements during the TARA transpolar drift 2006–2008. *Atmospheric Chemistry and Physics*, *9*(14), 4545–4557. <https://doi.org/10.5194/acp-9-4545-2009>

Burd, J. A., Peterson, P. K., Nghiem, S. V., Perovich, D. K., & Simpson, W. R. (2017). Snowmelt onset hinders bromine monoxide heterogeneous recycling in the Arctic. *Journal of Geophysical Research: Atmospheres*, *122*, 8297–8309. <https://doi.org/10.1002/2017JD026906>

Choi, S., Theys, N., Salawitch, R. J., Wales, P. A., Joiner, J., Canty, T. P., et al. (2018). Link between Arctic tropospheric BrO explosion observed from space and sea-salt aerosols from blowing snow investigated using ozone monitoring instrument BrO data and GEOS-5 data assimilation system. *Journal of Geophysical Research: Atmospheres*, *123*, 6954–6983. <https://doi.org/10.1029/2017JD026889>

Cole, A. S., & Steffen, A. (2010). Trends in long-term gaseous mercury observations in the Arctic and effects of temperature and other atmospheric conditions. *Atmospheric Chemistry and Physics*, *10*(10), 4661–4672. <https://doi.org/10.5194/acp-10-4661-2010>

Croft, B., Martin, R. V., Leaitch, W. R., Tunved, P., Breider, T. J., D'Andrea, S. D., & Pierce, J. R. (2016). Processes controlling the annual cycle of Arctic aerosol number and size distributions. *Atmospheric Chemistry and Physics*, *16*(6), 3665–3682. <https://doi.org/10.5194/acp-16-3665-2016>

Custard, K. D., Raso, A. R. W., Shepson, P. B., Staebler, R. M., & Pratt, K. A. (2017). Production and release of molecular bromine and chlorine from the Arctic coastal snowpack. *ACS Earth and Space Chemistry*, *1*(3), 142–151. <https://doi.org/10.1021/acsearthspacechem.7b00014>

Danckaert, T., Fayt, C., Van Roozendael, M., De Smedt, I., Letocart, V., Merlaud, A., & Pinardi, G. (2017). QDOAS Software user manual. Belgian Institute for Space Aeronomy (3.2 ed.) [Computer software manual].

Domine, F., Sparapani, R., Ianniello, A., & Beine, H. J. (2004). The origin of sea salt in snow on Arctic sea ice and in coastal regions. *Atmospheric Chemistry and Physics*, *4*(9/10), 2259–2271. <https://doi.org/10.5194/acp-4-2259-2004>

Douglas, T. A., & Sturm, M. (2004). Arctic haze, mercury and the chemical composition of snow across northwestern Alaska. *Atmospheric Environment*, *38*(6), 805–820. <https://doi.org/10.1016/j.atmosenv.2003.10.042>

Eigen, M., & Kustin, K. (1962). The kinetics of halogen hydrolysis. *Journal of the American Chemical Society*, *84*(8), 1355–1361. <https://doi.org/10.1021/ja00867a005>

Fan, S.-M., & Jacob, D. J. (1992). Surface ozone depletion in Arctic spring sustained by bromine reactions on aerosols. *Nature*, *359*, 522–524. <https://doi.org/10.1038/359522a0>

- Fogal, P. F., LeBlanc, L. M., & Drummond, J. R. (2013). The Polar Environment Atmospheric Research Laboratory (PEARL): Sounding the atmosphere at 80° north. *Arctic*, *66*(3), 377–386. <https://doi.org/10.2307/23594645>
- Foster, K. L., Plastringer, R. A., Bottenheim, J. W., Shepson, P. B., Finlayson-Pitts, B. J., & Spicer, C. W. (2001). The role of Br₂ and BrCl in surface ozone destruction at polar sunrise. *Science*, *291*(5503), 471–474. <https://doi.org/10.1126/science.291.5503.471>
- Fraser, A., Adams, C., Drummond, J. R., Goutail, F., Manney, G., & Strong, K. (2009). The polar environment atmospheric research laboratory UV–visible ground-based spectrometer: First measurements of O₃, NO₂, BrO, and OCIO columns. *Journal of Quantitative Spectroscopy and Radiative Transfer*, *110*(12), 986–1004. <https://doi.org/10.1016/j.jqsrt.2009.02.034>
- Frey, M. M., Norris, S. J., Brooks, I. M., Anderson, P. S., Nishimura, K., Yang, X., et al. (2020). First direct observation of sea salt aerosol production from blowing snow above sea ice. *Atmospheric Chemistry and Physics*, *20*(4), 2549–2578. <https://doi.org/10.5194/acp-20-2549-2020>
- Frieß, U., Sihler, H., Sander, R., Pöhler, D., Yilmaz, S., & Platt, U. (2011). The vertical distribution of BrO and aerosols in the Arctic: Measurements by active and passive differential optical absorption spectroscopy. *Journal of Geophysical Research*, *116*, D00R04. <https://doi.org/10.1029/2011JD015938>
- Gilman, J. B., Burkhart, J. F., Lerner, B. M., Williams, E. J., Kuster, W., Goldan, P. D., et al. (2010). Ozone variability and halogen oxidation within the Arctic and sub-Arctic springtime boundary layer. *Atmospheric Chemistry and Physics*, *10*(21), 10,223–10,236. <https://doi.org/10.5194/acp-10-10223-2010>
- Giordano, M. R., Kalnajs, L. E., Goetz, J. D., Avery, A. M., Katz, E., May, N. W., et al. (2018). The importance of blowing snow to halogen-containing aerosol in coastal Antarctica: Influence of source region versus wind speed. *Atmospheric Chemistry and Physics*, *18*(22), 16,689–16,711. <https://doi.org/10.5194/acp-18-16689-2018>
- Halfacre, J. W., Knepp, T. N., Shepson, P. B., Thompson, C. R., Pratt, K. A., Li, B., et al. (2014). Temporal and spatial characteristics of ozone depletion events from measurements in the Arctic. *Atmospheric Chemistry and Physics*, *14*(10), 4875–4894. <https://doi.org/10.5194/acp-14-4875-2014>
- Hall, D. K., & Riggs, G. A. (2015a). MODIS/Aqua Sea Ice Extent Daily L3 Global 1km EASE-Grid Day, Version 6 [March to May, 2016 to 2019]. NASA National Snow and Ice Data Center, Boulder, Colorado USA. Accessed: 09/09/2019, <https://doi.org/10.5067/MODIS/MYD29P1D.006>
- Hall, D. K., & Riggs, G. A. (2015b). MODIS/Terra Sea Ice Extent Daily L3 Global 1km EASE-Grid Day, Version 6 [March to May, 2016 to 2019]. NASA National Snow and Ice Data Center, Boulder, Colorado USA. Accessed: 09/09/2019, <https://doi.org/10.5067/MODIS/MOD29P1D.006>
- Hara, K., Matoba, S., Hirabayashi, M., & Yamasaki, T. (2017). Frost flowers and sea-salt aerosols over seasonal sea-ice areas in northwestern Greenland during winter-spring. *Atmospheric Chemistry and Physics*, *17*(13), 8577–8598. <https://doi.org/10.5194/acp-17-8577-2017>
- Hara, K., Osada, K., Matsunaga, K., Iwasaka, Y., Shibata, T., & Furuya, K. (2002). Atmospheric inorganic chlorine and bromine species in Arctic boundary layer of the winter/spring. *Journal of Geophysical Research*, *107*(D18), 4361. <https://doi.org/10.1029/2001JD001008>
- Hara, K., Osada, K., Yabuki, M., Takashima, H., Theys, N., & Yamanouchi, T. (2018). Important contributions of sea-salt aerosols to atmospheric bromine cycle in the Antarctic coasts. *Scientific Reports*, *8*(1), 13,852. <https://doi.org/10.1038/s41598-018-32287-4>
- Helmig, D., Boylan, P., Johnson, B., Oltmans, S., Fairall, C., Staebler, R., et al. (2012). Ozone dynamics and snow-atmosphere exchanges during ozone depletion events at Barrow, Alaska. *Journal of Geophysical Research*, *117*, D20303. <https://doi.org/10.1029/2012JD017531>
- Hönninger, G., Friedeburg, C., & Platt, U. (2004). Multi axis differential optical absorption spectroscopy (MAX-DOAS). *Atmospheric Chemistry and Physics*, *4*(1), 231–254. <https://doi.org/10.5194/acp-4-231-2004>
- Huang, J., & Jaeglé, L. (2017). Wintertime enhancements of sea salt aerosol in polar regions consistent with a sea ice source from blowing snow. *Atmospheric Chemistry and Physics*, *17*(5), 3699–3712. <https://doi.org/10.5194/acp-17-3699-2017>
- Huang, J., Jaeglé, L., & Shah, V. (2018). Using CALIOP to constrain blowing snow emissions of sea salt aerosols over Arctic and Antarctic sea ice. *Atmospheric Chemistry and Physics*, *18*, 16,253–16,269. <https://doi.org/10.5194/acp-18-16253-2018>
- Jacobi, H.-W., Morin, S., & Bottenheim, J. W. (2010). Observation of widespread depletion of ozone in the springtime boundary layer of the central Arctic linked to mesoscale synoptic conditions. *Journal of Geophysical Research*, *115*, D17302. <https://doi.org/10.1029/2010JD013940>
- Jones, A. E., Anderson, P. S., Begoin, M., Brough, N., Hutterli, M. A., Marshall, G. J., et al. (2009). BrO, blizzards, and drivers of polar tropospheric ozone depletion events. *Atmospheric Chemistry and Physics*, *9*(14), 4639–4652. <https://doi.org/10.5194/acp-9-4639-2009>
- Jones, A. E., Anderson, P. S., Wolff, E. W., Roscoe, H. K., Marshall, G. J., Richter, A., et al. (2010). Vertical structure of Antarctic tropospheric ozone depletion events: Characteristics and broader implications. *Atmospheric Chemistry and Physics*, *10*(16), 7775–7794. <https://doi.org/10.5194/acp-10-7775-2010>
- Kirpes, R. M., B. D., May, N. W., Fraund, M., Barget, A. J., Moffet, R. C., et al. (2019). Wintertime Arctic sea spray aerosol composition controlled by sea ice lead microbiology. *ACS Central Science*, *5*(11), 1760–1767. <https://doi.org/10.1021/acscentsci.9b00541>
- Leck, C., Norman, M., Bigg, E. K., & Hillamo, R. (2002). Chemical composition and sources of the high Arctic aerosol relevant for cloud formation. *Journal of Geophysical Research*, *107*(D12), AAC 1–1–AAC 1–17. <https://doi.org/10.1029/2001JD001463>
- Legrand, M., Yang, X., Preunkert, S., & Theys, N. (2016). Year-round records of sea salt, gaseous, and particulate inorganic bromine in the atmospheric boundary layer at coastal (Dumont d'Urville) and central (Concordia) East Antarctic sites. *Journal of Geophysical Research: Atmospheres*, *121*, 997–1023. <https://doi.org/10.1002/2015JD024066>
- Li, L., & Pomeroy, J. W. (1997). Estimates of threshold wind speeds for snow transport using meteorological data. *Journal of Applied Meteorology*, *36*(3), 205–213. [https://doi.org/10.1175/1520-0450\(1997\)036<0205:EOTWSF>2.0.CO;2](https://doi.org/10.1175/1520-0450(1997)036<0205:EOTWSF>2.0.CO;2)
- Liao, J., Huey, L. G., Tanner, D. J., Flocke, F. M., Orlando, J. J., Neuman, J. A., et al. (2012). Observations of inorganic bromine (HOBr, BrO, and Br₂) speciation at Barrow, Alaska, in spring 2009. *Journal of Geophysical Research: Atmospheres*, *117*, D00R16. <https://doi.org/10.1029/2011JD016641>
- Lieb-Lappen, R. M., & Obbard, R. W. (2015). The role of blowing snow in the activation of bromine over first-year Antarctic sea ice. *Atmospheric Chemistry and Physics*, *15*(13), 7537–7545. <https://doi.org/10.5194/acp-15-7537-2015>
- May, N. W., Quinn, P. K., McNamara, S. M., & Pratt, K. A. (2016). Multiyear study of the dependence of sea salt aerosol on wind speed and sea ice conditions in the coastal Arctic. *Journal of Geophysical Research: Atmospheres*, *121*, 9208–9219. <https://doi.org/10.1002/2016JD025273>
- McClure-Begley, A., Petropavlovskikh, I., & Oltmans, S. (2014). NOAA Global Monitoring Surface Ozone Network. 1973–2014. Accessed: 20/07/2020 <https://doi.org/10.7289/V57P8WBF>
- Nawrot, A. P., Migala, K., Luks, B., Pakszys, P., & Glowacki, P. (2016). Chemistry of snow cover and acidic snowfall during a season with a high level of air pollution on the Hans Glacier, Spitsbergen. *Polar Science*, *10*(3), 249–261. <https://doi.org/10.1016/j.polar.2016.06.003>

- Nghiem, S. V., Rigor, I. G., Richter, A., Burrows, J. P., Shepson, P. B., Bottenheim, J., et al. (2012). Field and satellite observations of the formation and distribution of Arctic atmospheric bromine above a rejuvenated sea ice cover. *Journal of Geophysical Research*, *117*, D00S05. <https://doi.org/10.1029/2011JD016268>
- Nilsson, E. D., Rannik, U., Swietlicki, E., Leck, C., Aalto, P. P., Zhou, J., & Norman, M. (2001). Turbulent aerosol fluxes over the Arctic Ocean: 2. Wind-driven sources from the sea. *Journal of Geophysical Research*, *106*(D23), 32,139–32,154. <https://doi.org/10.1029/2000JD900747>
- Oltmans, S. J., & Komhyr, W. D. (1986). Surface ozone distributions and variations from 1973–1984: Measurements at the NOAA Geophysical Monitoring for Climatic Change Baseline Observatories. *Journal of Geophysical Research*, *91*(D4), 5229–5236. <https://doi.org/10.1029/JD091iD04p05229>
- Payne, V. H., Clough, S. A., Shephard, M. W., Nassar, R., & Logan, J. A. (2009). Information-centered representation of retrievals with limited degrees of freedom for signal: Application to methane from the Tropospheric Emission Spectrometer. *Journal of Geophysical Research*, *114*, D10307. <https://doi.org/10.1029/2008JD010155>
- Peterson, P. K., Hartwig, M., May, N. W., Schwartz, E., Rigor, I., Ermold, W., et al. (2019). Snowpack measurements suggest role for multi-year sea ice regions in Arctic atmospheric bromine and chlorine chemistry. *Elementa (Washington, DC)*, *7*(1), 14. <https://doi.org/10.1525/elementa.352>
- Peterson, P. K., Pöhler, D., Sihler, H., Zielcke, J., General, S., Frieß, U., et al. (2017). Observations of bromine monoxide transport in the Arctic sustained on aerosol particles. *Atmospheric Chemistry and Physics*, *17*(12), 7567–7579. <https://doi.org/10.5194/acp-17-7567-2017>
- Peterson, P. K., Pöhler, D., Zielcke, J., General, S., Frieß, U., Platt, U., et al. (2018). Springtime bromine activation over coastal and inland Arctic snowpacks. *ACS Earth and Space Chemistry*, *2*(10), 1075–1086. <https://doi.org/10.1021/acsearthspacechem.8b00083>
- Peterson, P. K., Simpson, W. R., & Nghiem, S. V. (2016). Variability of bromine monoxide at Barrow, Alaska, over four halogen activation (March–May) seasons and at two on-ice locations. *Journal of Geophysical Research: Atmospheres*, *121*, 1381–1396. <https://doi.org/10.1002/2015JD024094>
- Peterson, P. K., Simpson, W. R., Pratt, K. A., Shepson, P. B., Frieß, U., Zielcke, J., et al. (2015). Dependence of the vertical distribution of bromine monoxide in the lower troposphere on meteorological factors such as wind speed and stability. *Atmospheric Chemistry and Physics*, *15*(4), 2119–2137. <https://doi.org/10.5194/acp-15-2119-2015>
- Pisso, I., Sollum, E., Grythe, H., Kristiansen, N., Cassiani, M., Eckhardt, S., et al. (2019). The Lagrangian particle dispersion model FLEXPART version 10.3. *Geoscientific Model Development Discussions*, *2019*, 1–67. <https://doi.org/10.5194/gmd-2018-333>
- Pöhler, D., Vogel, L., Frieß, U., & Platt, U. (2010). Observation of halogen species in the Amundsen Gulf, Arctic, by active long-path differential optical absorption spectroscopy. *Proceedings of the National Academy of Sciences*, *107*(15), 6582–6587. <https://doi.org/10.1073/pnas.0912231107>
- Pratt, K. A., Custard, K. D., Shepson, P. B., Douglas, T. A., Pöhler, D., General, S., et al. (2013). Photochemical production of molecular bromine in Arctic surface snowpacks. *Nature Geoscience*, *6*(5), 351–356. <https://doi.org/10.1038/NNGEO1779>
- Quinn, P. K., Shaw, G., Andrews, E., Dutton, E. G., Ruoho-Airola, T., & Gong, S. L. (2007). Arctic haze: Current trends and knowledge gaps. *Tellus B: Chemical and Physical Meteorology*, *59*(1), 99–114. <https://doi.org/10.1111/j.1600-0889.2006.00236.x>
- Rodgers, C. D. (2000). *Inverse Methods for Atmospheric Sounding: Theory and Practice*. Singapore: World Scientific. 2.
- Rozañov, A., Rozañov, V., Buchwitz, M., Kokhanovsky, A., & Burrows, J. P. (2005). SCIATRAN 2.0—A new radiative transfer model for geophysical applications in the 175–2400 nm spectral region. *Advances in Space Research*, *36*(5), 1015–1019. <https://doi.org/10.1016/j.asr.2005.03.012>
- Saha, S., Moorthi, S., Wu, X., Wang, J., Nadiga, S., Tripp, P., et al. (2011). NCEP Climate Forecast System Version 2 (CFSv2) 6-hourly products. Research Data Archive at the National Center for Atmospheric Research, Computational and Information Systems Laboratory, Boulder, Colorado, USA Accessed: 05/09/2019 <https://doi.org/10.5065/D61C1TXF>
- Saiz-Lopez, A., & von Glasow, R. (2012). Reactive halogen chemistry in the troposphere. *Chemical Society Reviews*, *41*(19), 6448–6472. <https://doi.org/10.1039/C2CS35208G>
- Schroeder, W. H., Anlauf, K. G., Barrie, L. A., Lu, J. Y., Steffen, A., Schneeberger, D. R., & Berg, T. (1998). Arctic springtime depletion of mercury. *Nature*, *394*(6691), 331–332. <https://doi.org/10.1038/28530>
- Sharp, M., Skidmore, M., & Nienow, P. (2002). Seasonal and spatial variations in the chemistry of a high Arctic supraglacial snow cover. *Journal of Glaciology*, *48*(160), 149–158. <https://doi.org/10.3189/172756502781831683>
- Sihler, H., Platt, U., Beirle, S., Marbach, T., Kühl, S., Dörner, S., et al. (2012). Tropospheric BrO column densities in the Arctic derived from satellite: Retrieval and comparison to ground-based measurements. *Atmospheric Measurement Techniques*, *5*(11), 2779–2807. <https://doi.org/10.5194/amt-5-2779-2012>
- Simpson, W. R., Brown, S. S., Saiz-Lopez, A., Thornton, J. A., & von Glasow, R. (2015). Tropospheric halogen chemistry: Sources, cycling, and impacts. *Chemical reviews*, *115*(10), 4035–4062. <https://doi.org/10.1021/cr5006638>
- Simpson, W. R., Glasow, R., Riedel, K., Anderson, P., Ariya, P., Bottenheim, J., et al. (2007). Halogens and their role in polar boundary-layer ozone depletion. *Atmospheric Chemistry and Physics*, *7*(16), 4375–4418. <https://doi.org/10.5194/acp-7-4375-2007>
- Simpson, W. R., Peterson, P. K., Frieß, U., Sihler, H., Lampel, J., Platt, U., et al. (2017). Horizontal and vertical structure of reactive bromine events probed by bromine monoxide MAX-DOAS. *Atmospheric Chemistry and Physics*, *17*(15), 9291–9309. <https://doi.org/10.5194/acp-17-9291-2017>
- Spicer, C. W., Plastringer, R. A., Foster, K. L., Finlayson-Pitts, B. J., Bottenheim, J. W., Grannas, A. M., & Shepson, P. B. (2002). Molecular halogens before and during ozone depletion events in the Arctic at polar sunrise: Concentrations and sources. *Atmospheric Environment*, *36*(15–16), 2721–2731. [https://doi.org/10.1016/S1352-2310\(02\)00125-5](https://doi.org/10.1016/S1352-2310(02)00125-5)
- Steffen, A., Douglas, T., Amyot, M., Ariya, P., Aspö, K., Berg, T., et al. (2008). A synthesis of atmospheric mercury depletion event chemistry in the atmosphere and snow. *Atmospheric Chemistry and Physics*, *8*(6), 1445–1482. <https://doi.org/10.5194/acp-8-1445-2008>
- Stohl, A., Eckhardt, S., Forster, C., James, P., Spichtinger, N., & Seibert, P. (2002). A replacement for simple back trajectory calculations in the interpretation of atmospheric trace substance measurements. *Atmospheric Environment*, *36*(29), 4635–4648. [https://doi.org/10.1016/S1352-2310\(02\)00416-8](https://doi.org/10.1016/S1352-2310(02)00416-8)
- Stohl, A., Hittenberger, M., & Wotawa, G. (1998). Validation of the Lagrangian particle dispersion model FLEXPART against large-scale tracer experiment data. *Atmospheric Environment*, *32*(24), 4245–4264. [https://doi.org/10.1016/S1352-2310\(98\)00184-8](https://doi.org/10.1016/S1352-2310(98)00184-8)
- Swanson, W. F., Graham, K. A., Halfacre, J. W., Holmes, C. D., Shepson, P. B., & Simpson, W. R. (2020). Arctic reactive bromine events occur in two distinct sets of environmental conditions: A statistical analysis of 6 years of observations. *Journal of Geophysical Research: Atmospheres*, *125*, e2019JD032139. <https://doi.org/10.1029/2019JD032139>
- Tarasick, D. W., & Bottenheim, J. W. (2002). Surface ozone depletion episodes in the Arctic and Antarctic from historical ozonesonde records. *Atmospheric Chemistry and Physics*, *2*(3), 197–205. <https://doi.org/10.5194/acp-2-197-2002>

- Theys, N., Van Roozendaal, M., Hendrick, F., Yang, X., De Smedt, I., Richter, A., et al. (2011). Global observations of tropospheric BrO columns using GOME-2 satellite data. *Atmospheric Chemistry and Physics*, *11*(4), 1791–1811. <https://doi.org/10.5194/acp-11-1791-2011>
- Toom-Sauntry, D., & Barrie, L. A. (2002). Chemical composition of snowfall in the high Arctic: 1990–1994. *Atmospheric Environment*, *36*(15-16), 2683–2693. [https://doi.org/10.1016/S1352-2310\(02\)00115-2](https://doi.org/10.1016/S1352-2310(02)00115-2)
- Tremblay, S., Picard, J.-C., Bachelder, J. O., Lutsch, E., Strong, K., Fogal, P., et al. (2019). Characterization of aerosol growth events over Ellesmere Island during the summers of 2015 and 2016. *Atmospheric Chemistry and Physics*, *19*(8), 5589–5604. <https://doi.org/10.5194/acp-19-5589-2019>
- Tschudi, M., Meier, W. N., Stewart, J. S., Fowler, C., & Maslanik, J. (2019). EASE-Grid Sea Ice Age, Version 4 [March to May, 2016 to 2019]. NASA National Snow and Ice Data Center, Boulder, Colorado USA Accessed: 09/09/2019 <https://doi.org/10.5067/UTAV7490FEPB>
- Vicente-Luis, A., Tremblay, S., Dionne, J., Chang, R. Y.-W., Fogal, P., Leaitch, W. R., et al. (2020). In situ aerosol optical properties in the Canadian high Arctic in winter and spring from 2016 to 2019. In Preparation.
- Wagner, T., Beirle, S., Brauers, T., Deutschmann, T., Frieß, U., Hak, C., et al. (2011). Inversion of tropospheric profiles of aerosol extinction and HCHO and NO₂ mixing ratios from MAX-DOAS observations in Milano during the summer of 2003 and comparison with independent data sets. *Atmospheric Measurement Techniques*, *4*(12), 2685–2715. <https://doi.org/10.5194/amt-4-2685-2011>
- Wang, S., McNamara, S. M., Moore, C. W., Obrist, D., Steffen, A., Shepson, P. B., et al. (2019). Direct detection of atmospheric atomic bromine leading to mercury and ozone depletion. *Proceedings of the National Academy of Sciences*, *116*(29), 14,479–14,484. <https://doi.org/10.1073/pnas.1900613116>
- Wennberg, P. (1999). Bromine explosion. *Nature*, *397*(6717), 299–301. <https://doi.org/10.1038/16805>
- Wren, S. N., Donaldson, D. J., & Abbatt, J. P. D. (2013). Photochemical chlorine and bromine activation from artificial saline snow. *Atmospheric Chemistry and Physics*, *13*(19), 9789–9800. <https://doi.org/10.5194/acp-13-9789-2013>
- Yang, X., Pyle, J. A., & Cox, R. A. (2008). Sea salt aerosol production and bromine release: Role of snow on sea ice. *Geophysical Research Letters*, *35*, L16815. <https://doi.org/10.1029/2008GL034536>
- Yang, X., Pyle, J. A., Cox, R. A., Theys, N., & Van Roozendaal, M. (2010). Snow-sourced bromine and its implications for polar tropospheric ozone. *Atmospheric Chemistry and Physics*, *10*(16), 7763–7773. <https://doi.org/10.5194/acp-10-7763-2010>
- Yilmaz, S. (2012). Retrieval of atmospheric aerosol and trace gas vertical profiles using multi-axis differential optical absorption spectroscopy (Doctoral Dissertation), University of Heilderberg. <https://doi.org/10.11588/heidok.00013128>
- Zhao, X., Strong, K., Adams, C., Schofield, R., Yang, X., Richter, A., et al. (2016). A case study of a transported bromine explosion event in the Canadian high Arctic. *Journal of Geophysical Research: Atmospheres*, *121*, 457–477. <https://doi.org/10.1002/2015JD023711>
- Zhao, X., Weaver, D., Bognar, K., Manney, G., Millán, L., Yang, X., et al. (2017). Cyclone-induced surface ozone and HDO depletion in the Arctic. *Atmospheric Chemistry and Physics*, *17*(24), 14,955–14,974. <https://doi.org/10.5194/acp-17-14955-2017>